Single-cell characterization of the eukaryotic transcription cycle using live imaging and statistical inference

Jonathan Liu[1], **Donald Hansen**[2], **Elizabeth Eck**[3], **Yang Joon Kim**[3], **Meghan Turner**[3], **Simon Alamos**[4], **Hernan G. Garcia**[1,3,5,6*]

***For correspondence:**
hggarcia@berkeley.edu

[1]Department of Physics, University of California at Berkeley, Berkeley, CA, USA; [2]Institute of Pharmacy and Molecular Biotechnology, University of Heidelberg, Heidelberg, Germany; [3]Biophysics Graduate Group, University of California at Berkeley, Berkeley, CA, USA; [4]Department of Plant and Microbial Biology, University of California at Berkeley, Berkeley, CA, USA; [5]Department of Molecular and Cell Biology, University of California at Berkeley, Berkeley, CA, USA; [6]Institute for Quantitative Biosciences-QB3, University of California at Berkeley, Berkeley, CA, USA

Abstract The eukaryotic transcription cycle consists of three main steps: initiation, elongation, and cleavage of the nascent RNA transcript. Although each of these steps can be regulated as well as coupled with each other, their *in vivo* dissection has remained challenging because available experimental readouts lack sufficient spatiotemporal resolution to separate the contributions from each of these steps. Here, we describe a novel computational technique to simultaneously infer the effective parameters of the transcription cycle in real time and at the single-cell level using a two-color MS2/PP7 reporter gene and the developing fruit fly embryo as a case study. Our method enables detailed investigations into cell-to-cell variability in transcription-cycle parameters with high precision. These measurements, combined with theoretical modeling, reveal a significant variability in the elongation rate of individual RNA polymerase molecules. We further illustrate the power of this technique by uncovering a novel mechanistic connection between RNA polymerase density and nascent RNA cleavage efficiency. Thus, our approach makes it possible to shed light on the regulatory mechanisms in play during each step of the transcription cycle in individual, living cells at high spatiotemporal resolution.

Main Text

Introduction

The eukaryotic transcription cycle consists of three main steps: initiation, elongation, and cleavage of the nascent RNA transcript (Fig. 1A; ***Alberts*** (***2015***)). Crucially, each of these three steps can be controlled to regulate transcriptional activity. For example, binding of transcription factors to enhancers dictates initiation rates (***Spitz and Furlong, 2012***), modulation of elongation rates helps determine splicing efficiency (***De La Mata et al., 2003***), and regulation of cleavage controls aspects of 3′ processing such as alternative polyadenylation (***Tian and Manley, 2016***).

The steps of the transcription cycle can be coupled with each other. For example, elongation rates contribute to determining mRNA cleavage and RNA polymerase (RNAP) termination efficiency (**Pinto et al., 2011**; **Hazelbaker et al., 2013**; **Fong et al., 2015**; **Liu et al., 2017**), and functional linkages have been demonstrated between transcription initiation and termination (**Moore and Proudfoot, 2009**; **Mapendano et al., 2010**). Nonetheless, initiation, elongation, and transcript cleavage have largely been studied in isolation. In order to dissect the entire transcription cycle, it is necessary to develop a holistic approach that makes it possible to understand how the regulation of each step dictates mRNA production and to unearth potential couplings among these steps.

To date, the processes of the transcription cycle have mostly been studied in detail using *in vitro* approaches (**Bai et al., 2006**; **Herbert et al., 2008**) or genome-wide measurements that require the fixation of cellular material and lack the spatiotemporal resolution to uncover how the regulation of the transcription cycle unfolds in real time (**Roeder, 1991**; **Saunders et al., 2006**; **Muse et al., 2007**; **Core et al., 2008**; **Fuda et al., 2009**; **Churchman and Weissman, 2011**). Only recently has it become possible to dissect these processes in living cells and in their full dynamical complexity using tools such as MS2 or PP7 to fluorescently label nascent transcripts at single-cell resolution (**Bertrand et al., 1998**; **Golding et al., 2005**; **Chao et al., 2008**; **Larson et al., 2011a**). These technological advances have yielded insights into, for example, intrinsic transcriptional noise in yeast (**Hocine et al., 2013**), kinetic splicing effects in human cells (**Coulon et al., 2014**), elongation rates in *Drosophila melanogaster* (**Garcia et al., 2013**; **Fukaya et al., 2017**), and transcriptional bursting in mammalian cells (**Tantale et al., 2016**), *Dictyostelium* (**Chubb et al., 2006**; **Muramoto et al., 2012**; **Corrigan and Chubb, 2014**), fruit flies (**Garcia et al., 2013**; **Lucas et al., 2013**; **Bothma et al., 2014**; **Fukaya et al., 2016**; **Falo-Sanjuan et al., 2019**; **Lammers et al., 2020**) and *Caenorhabditis elegans* (**Lee et al., 2019**).

Despite the great promise of MS2 and PP7, using these techniques to comprehensively analyze the transcription cycle is hindered by the fact that the signal from these *in vivo* RNA-labeling technologies convolves contributions from all aspects of the cycle. Specifically, the fluorescence signal from nascent RNA transcripts persists throughout the entire cycle of transcript initiation, elongation, and cleavage; further, a single gene can carry many tens of transcripts. Thus, at any given point, an MS2 or PP7 signal reports on the contributions of transcripts in various stages of the transcription cycle (**Ferraro et al., 2016**). Precisely interpreting an MS2 or PP7 signal therefore demands an integrated approach that accounts for this complexity.

Here, we present a method for analyzing live-imaging data from the MS2 and PP7 techniques in order to dynamically characterize the steps—initiation, elongation, and cleavage— of the full transcription cycle at single-cell resolution. This method combines a dual-color MS2/PP7 fluorescent reporter (**Hocine et al., 2013**; **Coulon et al., 2014**; **Fukaya et al., 2017**) with statistical inference techniques and quantitative modeling. As a proof of principle, we applied this analysis to the transcription cycle of a *hunchback* reporter gene in the developing embryo of the fruit fly *Drosophila melanogaster*. We validate our approach by comparing our inferred average initiation and elongation rates with previously reported results.

Crucially, our analysis also delivered novel single-cell statistics of the whole transcription cycle that were previously unmeasurable using genome-wide approaches, making it possible to generate distributions of parameter values necessary for investigations that go beyond simple population-averaged analyses (**Raj et al., 2006**; **Zenklusen et al., 2008**; **Sanchez et al., 2011**; **Coulon et al., 2013**; **Little et al., 2013**; **Sanchez et al., 2013**; **Sanchez and Golding, 2013**; **Jones et al., 2014**; **Serov et al., 2017**; **Lucas et al., 2018**; **Zoller et al., 2018**; **Ali et al., 2020**). We show that, by taking advantage of time-resolved data, our inference is able to filter out experimental noise in these distributions and retain sources of biological variability. By combining these statistics with theoretical models, we revealed substantial variability in RNAP stepping rates between individual molecules, demonstrating

the utility of our approach for testing hypotheses of the molecular mechanisms underlying the transcription cycle and its regulation.

This unified analysis enabled us to investigate couplings between the various transcription cycle parameters at the single-cell level, whereby we discovered a surprising correlation of cleavage rates with nascent transcript densities. These discoveries illustrate the potential of our method to sharpen hypotheses of the molecular processes underlying the regulation of the transcription cycle and to provide a framework for testing those hypotheses.

Results

To quantitatively dissect the transcription cycle in its entirety from live imaging data, we developed a simple model (Fig. 1A) in which RNAP molecules are loaded at the promoter of a gene of total length L with a time-dependent loading rate $R(t)$. For simplicity, we assume that each individual RNAP molecule behaves identically and independently: there are no interactions between molecules. While this assumption is a crude simplification, it nevertheless allows us to infer effective average transcription cycle parameters. We parameterize this $R(t)$ as the sum of a constant term $\langle R \rangle$ that represents the mean, or time-averaged, rate of initiation, and a small fluctuation term given by $\delta R(t)$ such that $R(t) = \langle R \rangle + \delta R(t)$. After initiation, each RNAP molecule traverses the gene at a constant, uniform elongation rate v_{elon}. Upon reaching the end of the gene, there follows a deterministic cleavage time, τ_{cleave}, after which the nascent transcript is cleaved. We do not consider RNAP molecules that do not productively initiate transcription (***Darzacq et al., 2007***) or that are paused at the promoter (***Core et al., 2008***), as they will provide no experimental readout. Based on experimental evidence (***Garcia et al., 2013***), we assume that these RNAP molecules are processive, such that each molecule successfully completes transcription, with no loss of RNAP molecules before the end of the gene (see Section S5 for a validation of this hypothesis).

Dual-color reporter for dissecting the transcription cycle

Here we studied the transcription cycle of early embryos of the fruit fly *D. melanogaster*. We focused on the P2 minimal enhancer and promoter of the *hunchback* gene during the 14th nuclear cycle of development; the gene is transcribed in a step-like pattern along the anterior-posterior axis of the embryo with a 26-fold modulation in overall mRNA count between the anterior and posterior end (Fig. 1B; ***Driever and Nusslein-Volhard*** (***1989***); ***Margolis et al.*** (***1995***); ***Perry et al.*** (***2012***); ***Garcia et al.*** (***2013***)). As a result, the fly embryo provides a natural modulation in mRNA production rates, with the position along the anterior-posterior axis serving as a proxy for mRNA output.

To visualize the transcription cycle, we utilized the MS2 and PP7 systems for live imaging of nascent RNA production (***Garcia et al., 2013***; ***Lucas et al., 2013***; ***Fukaya et al., 2016***). Using a two-color reporter construct similar to that reported in ***Hocine et al.*** (***2013***), ***Coulon et al.*** (***2014***), and ***Fukaya et al.*** (***2017***), we placed the MS2 and PP7 stem loop sequences in the 5' and 3' ends, respectively, of a transgenic *hunchback* reporter gene (Fig. 1C; see Fig. S1A for full construct details). The *lacZ* sequence and a portion of the *lacY* sequence from *Escherichia coli* were placed as a neutral spacer (***Chen et al., 2012***) between the MS2 and PP7 stem loops. As an individual RNAP molecule transcribes through a set of MS2/PP7 stem loops, constitutively expressed MCP-mCherry and PCP-GFP fusion proteins bind their respective stem loops, resulting in sites of nascent transcript formation that appear as fluorescent puncta under a laser-scanning confocal microscope (Fig. 2A and Video S1). The intensity of the puncta in each color channel is linearly related to the number of actively transcribing RNAP molecules that have elongated past the location of the associated stem loop sequence (***Garcia et al., 2013***), albeit with different arbitrary fluorescence units (Section S4). Upon reaching the end of the gene, which contains the 3'UTR of the *α-tubulin* gene (***Chen et al., 2012***), the nascent RNA transcript undergoes cleavage. Because the characteristic

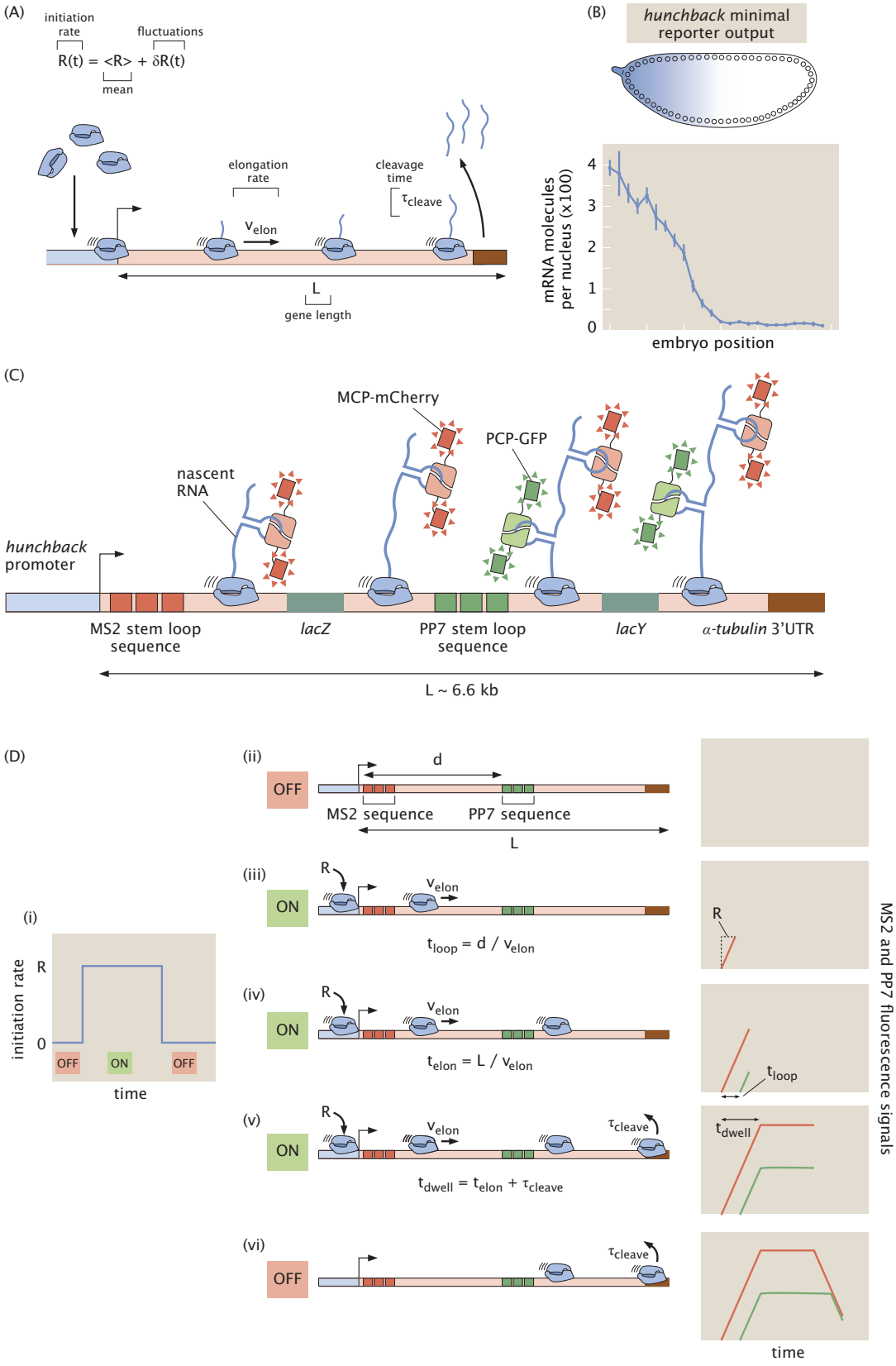

Figure 1. Overview of theoretical model of the transcription cycle and experimental setup. See caption on next page.

Figure 1. Overview of theoretical model of the transcription cycle and experimental setup. (A) Simple model of the transcription cycle, incorporating nascent RNA initiation, elongation, and cleavage. (B) The reporter construct, which is driven by the *hunchback* P2 minimal enhancer and promoter, is expressed in a step-like fashion along the anterior-posterior axis of the fruit fly embryo. (C) Transcription of the stem loops results in fluorescent puncta with the 5′ mCherry signal appearing before the signal from 3′ GFP. Only one stem loop per fluorophore is shown for clarity, but the actual construct contains 24 repeats. (D) Intuition for how MS2 and PP7 fluorescence depend on the model parameters. (i) Example transcription activity that consists of a pulse of transcription initiation of constant magnitude R. (ii) At first, the zero initiation rate results in no fluorescence. (iii) When initiation commences, RNAP molecules load onto the promoter and elongation of nascent transcripts occurs, resulting in a constant increase in the MS2 signal. (iv) After time $t_{loop} = \frac{d}{v_{elon}}$, the first RNAP molecules reach the PP7 stem loops and the PP7 signal also increases at a constant rate. (v) After time $t_{elon} = \frac{L}{v_{elon}}$, the first RNAP molecules reach the end of the gene, and after the cleavage time τ_{cleave}, these first nascent transcripts are cleaved. The total time a nascent RNA transcript spends on the gene is given by $t_{dwell} = t_{elon} + \tau_{cleave}$. The subsequent loss of fluorescence is balanced by the addition of new nascent transcripts, resulting in a plateauing of the signal. (vi) Once the initiation rate shuts off, no new RNAP molecules are added and the overall fluorescence signal starts to decrease due to cleavage of the nascent transcripts still on the gene. Data in (B) adapted from ***Garcia et al.*** (***2013***); the line represents the mean and error bars represent standard error across 24 embryos.

timescale of mRNA diffusion is about two order of magnitudes faster than the time resolution of our experiment, we approximate the cleavage of a single transcript as resulting in the instantaneous loss of its associated fluorescent signal in both channels (Section S2). The qualitative relationship between the model parameters and the fluorescence data is described in Figure 1D, which considers the case of a pulse of constant initiation rate.

Transcription cycle parameter inference using Markov Chain Monte Carlo

Our statistical framework extracts quantitative estimates of transcription-cycle parameters (Fig. 1A) from fluorescence signals. From microscopy data (Fig. 2A and Video S1), time traces of mCherry and eGFP fluorescence intensity are extracted to produce a dual-signal readout of nascent RNA transcription at single-cell resolution (Fig. 2B, data points). To extract quantitative insights from the observed fluorescence data, we used the established Bayesian inference technique of Markov Chain Monte Carlo (MCMC) (***Geyer*** (***1992***) and Section S3.1) to infer the effective parameter values in our simple model of transcription: the time-dependent transcription initiation rate, separated into the constant term $\langle R \rangle$ and fluctuations $\delta R(t)$, the elongation rate v_{elon}, and the cleavage time τ_{cleave}. We included a few additional free parameters: basal levels of fluorescence in each channel, the time of transcription onset after the previous mitosis, and the scaling factor between the arbitrary fluorescence units of the two different fluorophores (Section S1 and S3.1). Altogether, the model produced the best-fit to the data shown in Figure 2B. The inference was run at the single-cell level, resulting in separate parameter estimates for each cell. Additionally, we used a two-step process to sequentially determine parameters with higher accuracy (Section S3.2). Inference results were filtered both automatically and via manual curation to disregard results that were obscured by experimental limitations such as incomplete fluorescent signals; this curation process did not substantially affect the ultimate inference results (Section S3.3 and Fig. S3). To aggregate the results, we constructed a distribution from the single-cell results for each inferred parameter. Intra-embryo variability between single cells was greater than inter-embryo variability (Section S6 and Fig. S6). As a result, unless stated otherwise, all statistics reported here were aggregated across single cells combined between embryos, and all shaded errors reflect the standard error of the mean.

The aggregated inference results produced a suite of quantitative measurements of transcription initiation, elongation, and cleavage dynamics for the *hunchback* reporter gene as a function of the position along the anterior-posterior axis of the embryo (Fig. 2C-H), as well as an inferred

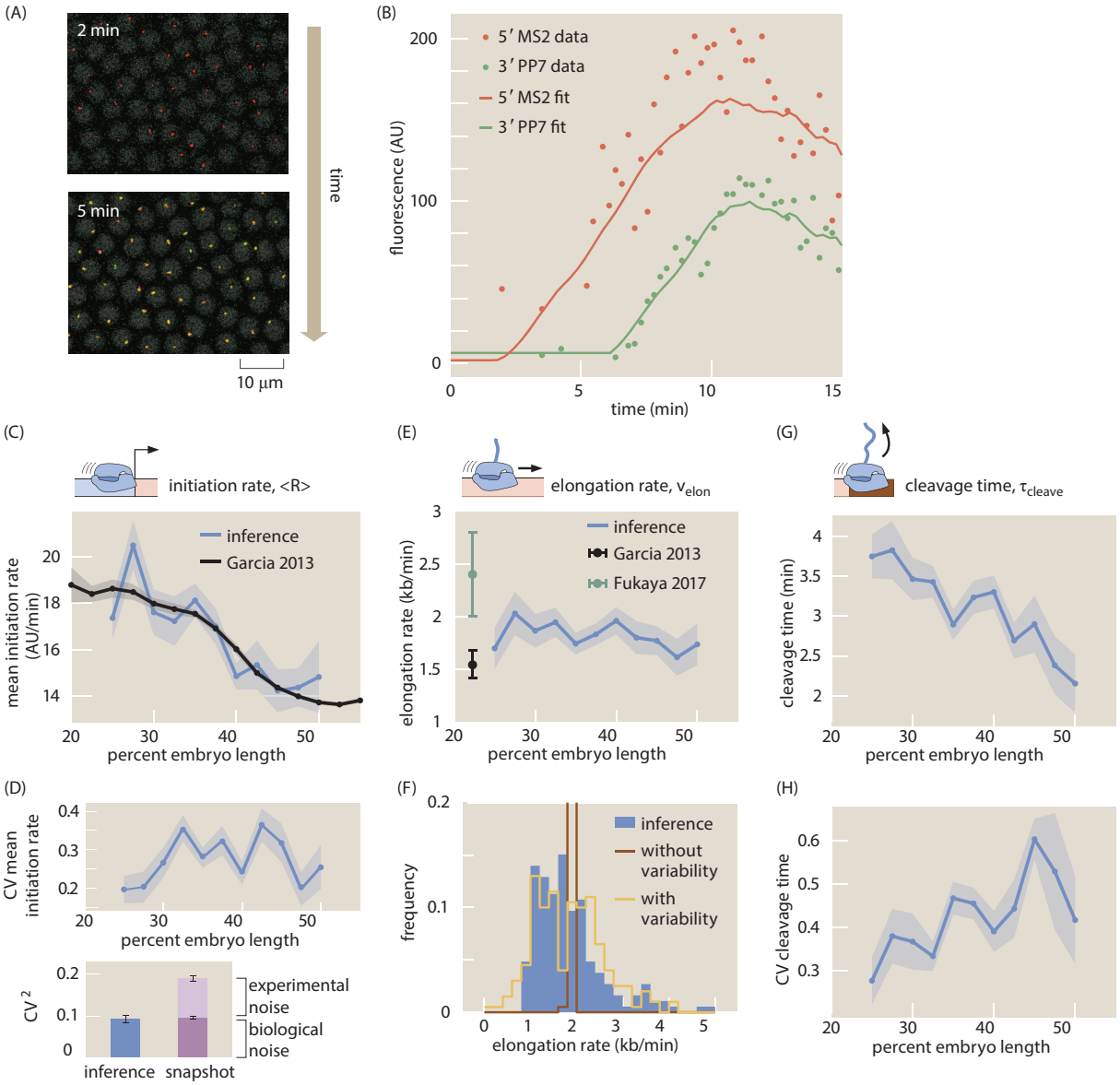

Figure 2. Inferred transcription-cycle parameters. (A) Snapshots of confocal microscopy data over time, with MS2-mCherry (red) and PP7-eGFP (green) puncta corresponding to transcription activity. (B) Sample single-cell MS2 and PP7 fluorescence (points) together with best-fits of the model using MCMC inference (curves). (C) Mean inferred transcription initiation rate as a function of embryo position (blue), along with rescaled, previously reported results (black, ***Garcia et al.*** (***2013***)). (D, top) CV of mean initiation rate along the embryo. (D, bottom) Comparison of the squared CV of mean initiation rate inferred using our approach (blue) or obtained from examining the fluorescence of transcription spots in a single snapshot (purple). While snapshots captured a significant amount of experimental noise (light purple), our inference accounts mostly for biological noise (blue vs. dark purple). See Section S7 and Fig. S7 for details. (E) Inferred elongation rate as a function of embryo position, along with previously reported results (black, ***Garcia et al.*** (***2013***); teal, ***Fukaya et al.*** (***2017***)). (F) Distribution of inferred single-cell elongation rates in the anterior 40% of embryo (blue), along with best fit to mean and standard deviation using single-molecule simulations with and without RNAP-to-RNAP variability (gold and brown, respectively). Although the distribution of the brown curve approaches 1, the y-axis here is cut off at 0.2 for ease of visualization. (G) Inferred cleavage time as a function of embryo position. (H) CV of cleavage time as a function of embryo position. (C,E,G, shaded error reflects standard error of the mean across 299 nuclei in 7 embryos, or of previously reported mean results; D,H, shaded error or black error bars represent bootstrapped standard errors of the CV or CV^2 for 100 bootstrap samples each; E, error bars reflect standard error of the mean for ***Garcia et al.*** (***2013***) and lower (25%) and upper (75%) quintiles of the full distribution from ***Fukaya et al.*** (***2017***).)

scaling factor between the mCherry and eGFP fluorescence units (Section S4 and Fig. S5). This inferred fluorescence scaling factor agreed with an independent calibration control experiment (Section S4 and Fig. S5), showing that our methodology calibrates the intensities of distinct fluorescent proteins without resorting to independent control experiments. Furthermore, investigations with simulated data validated the accuracy of our inference method (Section S3.4 and Fig. S4).

Inference of single-cell initiation rates recapitulates and improves on previous measurements

Control of initiation rates is one of the predominant, and as a result most well-studied, strategies for gene regulation (***Roeder, 1991***; ***Spitz and Furlong, 2012***; ***Lenstra et al., 2016***). Thus, comparing our inferred initiation rates with previously established results comprised a crucial benchmark for our methodology. Our inferred values of the mean initiation rate $\langle R \rangle$ exhibited a step-like pattern along the anterior-posterior axis of the embryo, qualitatively reproducing the known *hunchback* expression profile (Fig. 2C, blue). As a point of comparison, we also examined the mean initiation rate measured by ***Garcia et al.*** (***2013***), which was obtained by manually fitting a trapezoid (Figure 1D) to the average MS2 signal (Fig. 2C, black). The quantitative agreement between these two dissimilar analysis methodologies demonstrates that our inference method can reliably extract the average rate of transcription initiation across cells.

Measurements of cell-to-cell variability in transcription initiation rate have uncovered, for example, the existence of transcriptional bursting and mechanisms underlying the establishment of precise developmental boundaries (***Raj et al., 2006***; ***Sanchez and Golding, 2013***; ***Zenklusen et al., 2008***; ***Little et al., 2013***; ***Jones et al., 2014***; ***Lucas et al., 2018***; ***Zoller et al., 2018***). Yet, to date, these studies have mostly employed techniques such as single-molecule FISH to count the number of nascent transcripts on a gene or the number of cytoplasmic mRNA molecules (***Femino et al., 1998***; ***Raj et al., 2006***; ***Pare et al., 2009***; ***Zenklusen et al., 2008***; ***So et al., 2011***; ***Boettiger and Levine, 2013***; ***Little et al., 2013***; ***Jones et al., 2014***; ***Senecal et al., 2014***; ***Padovan-Merhar et al., 2015***; ***Xu et al., 2015***; ***Skinner et al., 2016***; ***Bartman et al., 2016***; ***Hendy et al., 2017***; ***Zoller et al., 2018***). In principle, these techniques do not report on the variability in transcription initiation alone; they convolve this measurement with variability in other steps of the transcription cycle (***Padovan-Merhar et al., 2015***; ***Lenstra et al., 2016***).

Our inference approach isolates the transcription initiation rate from the remaining steps of the transcription cycle at the single-cell level, making it possible to calculate, for example, the coefficient of variation (CV; standard deviation divided by the mean) of the mean rate of initiation. Our results yielded values for the CV along the embryo that peaked around 35% (Fig. 2D, top). This value is roughly comparable to that obtained for *hunchback* using single-molecule FISH (***Little et al., 2013***; ***Xu et al., 2015***; ***Zoller et al., 2018***).

One of the challenges in measuring CV values, however, is that informative biological variability is often convolved with undesired experimental noise. Although we currently cannot separate these sources with our data and inference method, a strategy for this separation was recently implemented in the context of snapshot-based fluorescent data (***Zoller et al., 2018***). Building on this strategy, we took a single snapshot from our live-imaging data and calculated the total squared CV of the fluorescence of spots at a single time point (Fig. 2D, bottom, purple).

Following ***Zoller et al.*** (***2018***) and as described in detail in Section S7 and Figure S7, we calculated the biological and experimental noise in this snapshot-based measurement. The bar graph shown in the bottom of Figure 2D shows that, once the experimental noise (light purple) is subtracted from the total noise of our snapshot-based measurement, the remaining biological variability (dark purple) is comparable to the variability of our inference results (blue). Thus, our inference mostly captures biological variability and filters out experimental noise, similarly to techniques such as

single-molecule FISH (**Zoller et al., 2018**) but with the added advantage of also being able to resolve temporal information. These results further validate our approach and demonstrate its capability to capture measures of cell-to-cell variability in the transcription cycle with high precision.

Elongation rate inference reveals single-molecule variability in RNAP stepping rates

Next, we investigated the ability of our inference approach to report on the elongation rate v_{elon}. Nascent RNA elongation plays a prominent role in gene regulation, for example, in dosage compensation in *Drosophila* embryos (**Larschan et al., 2011**), alternative splicing in human cells (**De La Mata et al., 2003**; **Batsché et al., 2006**), and gene expression in plants (**Wu et al., 2016**). Our method inferred an elongation rate v_{elon} that was constant along the embryo (Fig. 2E), lending support to previous reports indicating a lack of regulatory control of the elongation rate in the early fly embryo (**Fukaya et al., 2017**). We measured a mean elongation rate of 1.84 ± 0.04 kb/min (SEM; n = 299), consistent with previous measurements of the fly embryo (Fig. 2E, black and teal; **Garcia et al.** (**2013**); **Fukaya et al.** (**2017**)), as well as with measurements from other techniques and model organisms, which range from about 1 kb/min to upwards of 4 kb/min (**Golding et al., 2005**; **Darzacq et al., 2007**; **Boireau et al., 2007**; **Ardehali and Lis, 2009**; **Hocine et al., 2013**; **Coulon et al., 2014**; **Fuchs et al., 2014**; **Tantale et al., 2016**; **Lenstra et al., 2016**).

Like cell-to-cell variability in transcription initiation, single-cell distributions of elongation rates can provide crucial insights into, for example, promoter-proximal pausing (**Serov et al., 2017**), traffic jams (**Klumpp and Hwa, 2008**; **Klumpp, 2011**), transcriptional bursting (**Choubey et al., 2015**, **2018**), and noise propagation (**Ali et al., 2020**). While genome-wide approaches have had huge success in measuring mean properties of elongation (**Core et al., 2008**; **Carrillo Oesterreich et al., 2010**), they remain unable to resolve single-cell distributions of elongation rates. We examined the statistics of single-cell elongation rates in the anterior 40% of the embryo, where the initiation rate was roughly constant, and inferred a broad distribution with a standard deviation of around 0.5 kb/min and a long tail extending to values upwards of 4 kb/min (Fig. 2F, blue). This large spread was consistent with observations of large cell-cell variability in elongation rates (**Palangat and Larson, 2012**; **Lenstra et al., 2016**), as well as with measurements from similar two-color live imaging experiments (**Hocine et al.** (**2013**); **Fukaya et al.** (**2017**); Section S8; Fig. S8).

To illustrate the resolving power of examining elongation rate distributions, we performed theoretical investigations of elongation dynamics. Following **Klumpp and Hwa** (**2008**), we considered a model where RNAP molecules stochastically step along a gene and cannot overlap or pass each other (Section S9). First, we considered a scenario where the stepping rate of each RNAP molecule is identical. As shown in brown in Figure 2F, this model cannot account for the wide distribution of observed single-cell elongation rates. In contrast, the model can reasonably describe data by allowing for substantial variability in the elongation rate of individual RNAP molecules. As shown in gold in Figure 2F, the model can quantitatively approximate the inferred distribution. This single-molecule variability is consistent with *in vitro* observations of substantial molecule-to-molecule variability in RNAP elongation rates (**Tolić-Nørrelykke et al.** (**2004**); **Larson et al.** (**2011b**)), thus demonstrating the ability of our approach to engage in the *in vivo* dissection of the transcription cycle at the single-molecule level.

Inference reveals functional dependencies of cleavage times

Finally, we inferred values of the cleavage time τ_{cleave}. Through processes such as alternative polyadenylation (**Tian and Manley, 2016**; **Jung et al., 2009**) and promoter-terminator crosstalk (**Moore and Proudfoot, 2009**; **Mapendano et al., 2010**), events at the 3′ end of a gene exert substantial influence over overall transcription levels (**Bentley, 2014**). Although many investigations of mRNA cleavage and RNAP termination have been carried out in fixed-tissue samples (**Richard and**

Manley, 2009; ***Kuehner et al., 2011***), live-imaging studies with single-cell resolution of this important process remain sparse; some successes have been achieved in yeast and in mammalian cells (***Lenstra et al., 2016***). We inferred a mean mRNA cleavage time in the range of 2-4 min (Fig. 2G), consistent with values obtained from live imaging in yeast (***Larson et al., 2011a***) and mammalian cells (***Boireau et al., 2007***; ***Darzacq et al., 2007***; ***Coulon et al., 2014***; ***Tantale et al., 2016***). Interestingly, as shown in Figure 2G, the inferred mRNA cleavage time was strongly dependent on anterior-posterior positioning along the embryo, with high values (~4 min) in the anterior end and lower values toward the posterior end (~2 min). Such a modulation could not have been easily revealed using genome-wide approaches that, by necessity, average information across multiple cells. The CV of the cleavage time also increased toward the posterior end of the embryo (Fig. 2H), providing fertile ground for uncovering the molecular underpinnings of these processes using theoretical models analogous to those discussed previously. Thus, although cleavage remains an understudied process compared to initiation and elongation, both theoretically and experimentally, these results provide the quantitative precision necessary to carry out such mechanistic analyses.

Uncovering mechanistic correlations between transcription cycle parameters

In addition to revealing trends in average quantities of the transcription cycle along the length of the embryo, the simultaneous nature of the inference afforded us the unprecedented ability to investigate single-cell correlations between transcription-cycle parameters. The mean initiation rate and the cleavage time exhibited a slight negative linear correlation ([$R^2 = 0.10$, $p = 1 \times 10^{-8}$], Fig. 3A). This negative correlation at the single-cell level should be contrasted with the positive relation between these magnitudes at the position-averaged level, where the mean initiation rate and cleavage time both increased in the anterior of the embryo (Fig. 2C and G). Thus, our analysis unearthed a quantitative relationship that was obscured by a naive investigation of spatially averaged quantities, an approach often used in fixed (***Zoller et al., 2018***) and live-imaging (***Lammers et al., 2020***) studies, as well as in genome-wide investigations (***Combs and Eisen, 2017***; ***Haines and Eisen, 2018***). We also detected a small positive correlation ($R^2 = 0.09$, $p = 1 \times 10^{-7}$) between cleavage times and elongation rates (Fig. 3B). These results are consistent with prior studies implicating elongation rates in 3′ processes such as splicing and alternative polyadenylation: slower elongation rates increased cleavage efficiency (***De La Mata et al., 2003***; ***Pinto et al., 2011***). We detected no significant correlation ($R^2 = 0.01$, $p = 0.08$) between elongation rates and mean initiation rates (Fig. 3C).

The observed negative correlation between cleavage time and mean initiation rate (Fig. 3A), in conjunction with the positive correlation between cleavage time and elongation rate (Fig. 3B), suggested a potential underlying biophysical control parameter: the mean nascent transcript density on the reporter gene body ρ:

$$\rho = \frac{\langle R \rangle}{v_{elon}}. \tag{1}$$

Possessing units of (AU/kb), this mean transcript density estimates the average number of nascent RNA transcripts per kilobase of template DNA. Plotting the cleavage time as a function of the mean transcript density yielded a negative correlation that, while moderate ($R^2 = 0.18$, $p = 5 \times 10^{-15}$), was stronger than any of the previous correlations between transcription-cycle parameters (Fig. 3D). Mechanistically, this correlation suggests that, on average, more closely packed nascent transcripts at the 3′ end of a gene cleave faster. Further investigations using simulations indicated that these relationships did not arise from spurious correlations in the inference procedure itself (Section S3.4 and Fig. S4E-H), but rather captured real correlations in the data.

Using an absolute calibration for a similar reporter gene (***Garcia et al., 2013***) led to a rough scaling of 1 AU ≈ 1 molecule corresponding to a maximal RNAP density of 20 RNAP molecules/kb in Figure 3D. With a DNA footprint of 40 bases per molecule (***Selby et al., 1997***), this calculation

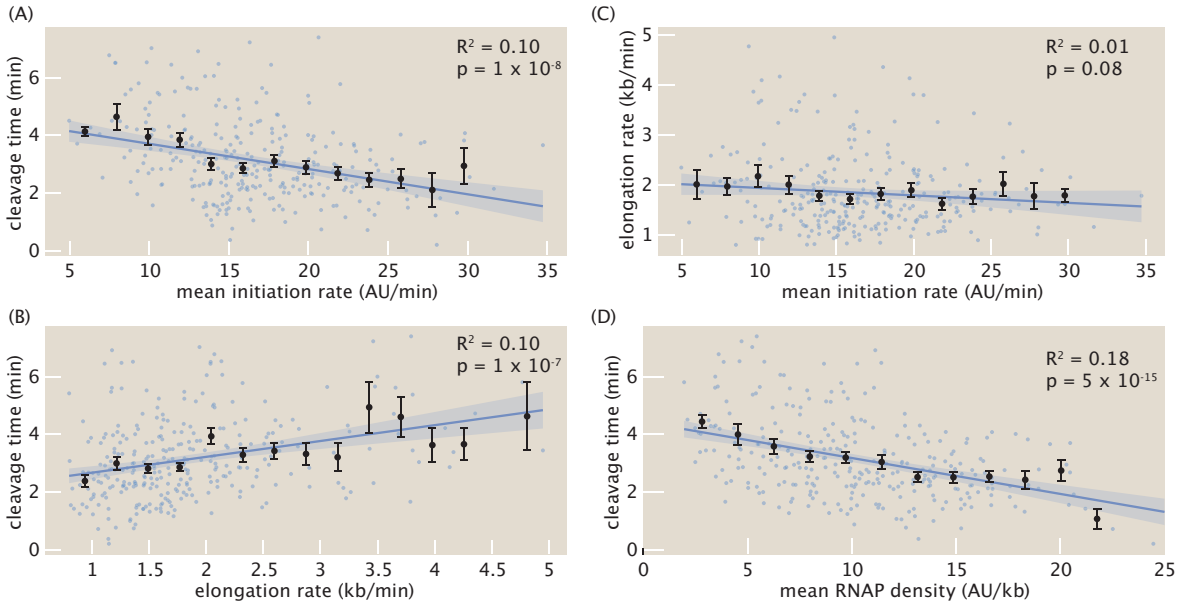

Figure 3. Single-cell correlations between transcription cycle parameters. Correlations between (A) mean initiation rate and cleavage time, (B) elongation rate and cleavage time, (C) mean initiation rate and elongation rate, and (D) mean RNAP density and cleavage time. Blue points indicate single-cell values; black points and error bars indicate mean and SEM, respectively, binned across x-axis values. Line and shaded region indicate generalized linear model fit and 95% confidence interval, respectively. Adjusted R^2 values and p-values were calculated using a generalized linear regression model (see Methods and Materials for details).

suggests that in this regime, the RNAP molecules are densely distributed enough to occupy 80% of the reporter gene. We hypothesize that increased RNAP density could lead to increased pausing as a result of traffic jams (***Klumpp and Hwa, 2008***; ***Klumpp, 2011***). Due to this pausing, transcripts would be more available for cleavage, increasing overall cleavage efficiency. Regardless of the particular molecular mechanisms underlying our observations, we anticipate that this ability to resolve single-cell correlations between transcription parameters, combined with perturbative experiments, will provide ample future opportunities for studying the underlying biophysical mechanisms linking transcription processes.

Discussion

Over the last two decades, the genetically encoded MS2 (***Bertrand et al., 1998***) and PP7 (***Chao et al., 2008***) RNA labeling technologies have made it possible to measure nascent and cytoplasmic RNA dynamics *in vivo* in many contexts (***Golding et al., 2005***; ***Chubb et al., 2006***; ***Darzacq et al., 2007***; ***Larson et al., 2011a***; ***Garcia et al., 2013***; ***Lucas et al., 2013***; ***Hocine et al., 2013***; ***Coulon et al., 2014***; ***Bothma et al., 2014***; ***Lenstra et al., 2016***; ***Fukaya et al., 2016***; ***Tantale et al., 2016***; ***Fukaya et al., 2017***; ***Chen et al., 2018***; ***Dufourt et al., 2018***; ***Fritzsch et al., 2018***; ***Falo-Sanjuan et al., 2019***; ***Li et al., 2019***; ***Lee et al., 2019***; ***Lammers et al., 2020***; ***Eck et al., 2020***). However, such promising experimental techniques can only be as powerful as their underlying data-analysis infrastructure. For example, while initial studies using MS2 set the technological foundation for revealing transcriptional bursts in bacteria (***Golding et al., 2005***), single-celled eukaryotes (***Chubb et al., 2006***; ***Larson et al., 2009***), and animals (***Garcia et al., 2013***; ***Lucas et al., 2013***), only recently did analysis techniques become available to reliably obtain parameters such as transcriptional burst frequency, duration, and amplitude (***Coulon et al., 2014***; ***Desponds et al., 2016***; ***Corrigan et al., 2016***; ***Lammers et al., 2020***).

In this work, we established a novel method for inferring quantitative parameters of the entire transcription cycle—initiation, elongation and cleavage—from live imaging data. Notably, this method offers high spatiotemporal resolution at the single-cell level. These features are unattainable by widespread, but still powerful, genome-wide techniques that examine fixed samples, such as global run-on sequencing (GRO-seq) to measure elongation rates *in vivo* (**Danko et al., 2013**; **Jonkers and Lis, 2015**).

From elucidating the nature of mutations (**Luria and Delbruck, 1943**) and revealing mechanisms of transcription initiation (**Zenklusen et al., 2008**; **Sanchez et al., 2011**; **So et al., 2011**; **Sanchez et al., 2013**; **Sanchez and Golding, 2013**; **Little et al., 2013**; **Hocine et al., 2013**; **Jones et al., 2014**; **Xu et al., 2015**; **Choubey et al., 2015**; **Zoller et al., 2018**; **Choubey et al., 2018**), transcription elongation (**Boettiger et al., 2011**; **Serov et al., 2017**; **Ali et al., 2020**), and translational control (**Cai et al., 2006**), to enabling the calibration of fluorescent proteins in absolute units (**Rosenfeld et al., 2005**, **2006**; **Teng et al., 2010**; **Brewster et al., 2014**; **Kim et al., 2016**; **Bakker and Swain, 2019**), examining single-cell distributions through the lens of theoretical models has made it possible to extract molecular insights about biological function that are inaccessible through the examination of averaged quantities. The single-cell measurements afforded by our approach made it possible to infer full distributions of transcription parameters (Fig. 2D, F, and H). This single-cell resolution motivates a dialogue between theory and experiment for studying transcription initiation, elongation, and cleavage at the single-cell level. Specifically, we showed how our inferred distributions of initiation rates effectively filter out experimental noise while retaining temporal information, and how elongation rate distributions make it possible to test molecular models of RNAP transit along the gene.

Finally, the simultaneous inference of various transcription-cycle parameters granted us the novel capability to investigate couplings between aspects of transcription initiation, elongation, and cleavage, paving the way for future studies of mechanistic linkages between these processes. In particular, the observed coupling of the mRNA cleavage time with RNAP density (Fig. 3D) suggests potential avenues for investigating mechanisms underlying this phenomenon, such as RNAP traffic jams (**Klumpp and Hwa, 2008**; **Klumpp, 2011**), inefficient or rate-limiting nascent RNA cleavage (**Fong et al., 2015**; **Jung et al., 2009**), and promoter-terminator looping (**Hampsey et al., 2011**).

Our statistical methodology can be readily applied beyond the regulation of a *hunchback* reporter in *Drosophila melanogaster* to other genes and organisms in which MS2 and PP7 have been already implemented (**Golding et al., 2005**; **Chubb et al., 2006**; **Darzacq et al., 2007**; **Garcia et al., 2013**; **Lucas et al., 2013**; **Tantale et al., 2016**; **Lee et al., 2019**; **Sato et al., 2020**), or where non-genetically encoded RNA aptamer technologies such as Spinach (**Paige et al., 2011**; **Sato et al., 2020**) are available. Further studies could extend this technique to account for bursty genes (**Rodriguez and Larson, 2020**), where the initiation rate fluctuates much more rapidly in time such that our assumption of a constant mean transcription initiation rate breaks down, or to encompass questions of intrinsic and extrinsic noise by performing inference on the transcriptional dynamics of two identical alleles (**Elowitz et al., 2002**; **Raser and O'Shea, 2004**; **Raj et al., 2006**). Finally, while our experimental setup utilized two fluorophores, we found that the calibration between their intensities could be inferred directly from the data (Section S4 and Fig. S5), rendering independent calibration and control experiments unnecessary. Thus, we envision that our analysis strategy will be of broad applicability to the quantitative and molecular *in vivo* dissection of the transcription cycle and its regulation across many distinct model systems.

Methods and Materials

DNA constructs

The fly strain used to express constitutive MCP-mCherry and PCP-eGFP consisted of two transgenic constructs. The first construct, MCP-NoNLS-mCherry, was created by replacing the eGFP in MCP-

NoNLS-eGFP (***Garcia et al., 2013***) with mCherry. The second construct, PCP-NoNLS-eGFP, was created by replacing MCP in the aforementioned MCP-NoNLS-eGFP with PCP, sourced from ***Larson et al.*** (***2011a***). Both constructs were driven with the *nanos* promoter to deliver protein maternally into the embryo. The constructs lacked nuclear localization sequences because the presence these sequences created spurious fluorescence puncta in the nucleus that decreased the overall signal quality (data not shown). Both constructs were incorporated into fly lines using P-element transgenesis, and a single stable fly line was created by combining all three transgenes.

The reporter construct P2P-MS2-lacZ-PP7 was cloned using services from GenScript, and was incorporated into a fly line using PhiC31-mediated Recombinase Mediated Cassette Exchange (RMCE), at the 38F1 landing site.

Full details of construct and sequence information can be found in a public Benchling folder.

Fly strains

Transcription of the *hunchback* reporter was measured by imaging embryos resulting from crossing *yw;MCP-NoNLS-mCherry,Histone-iRFP;MCP-NoNLS-mCherry,PCP-NoNLS-GFP* female virgins with *yw;P2P-MS2-LacZ-PP7* males. The *Histone-iRFP* transgene was provided as a courtesy from Kenneth Irvine and Yuanwang Pan.

Transcription from the *hunchback* promoter was measured by imaging embryos resulting from crossing female virgins *yw;HistoneRFP;MCP-NoNLS(2)* with male *yw;P2P-MS2-lacZ-PP7/cyo;+* (***Garcia et al., 2013***).

Sample preparation and data collection

Sample preparation followed procedures described in ***Bothma et al.*** (***2014***), ***Garcia and Gregor*** (***2018***), and ***Lammers et al.*** (***2020***). Embryos were collected and mounted in halocarbon oil 27 between a semipermeable membrane (Lumox film, Starstedt, Germany) and a coverslip. Data collection was performed using a Leica SP8 scanning confocal microscope (Leica Microsystems, Biberach, Germany). The MCP-mCherry, PCP-eGFP, and Histone-iRFP were excited with laser wavelengths of 488 nm, 587 nm, and 670 nm, respectively, using a White Light Laser. Average laser powers on the specimen (measured at the output of a 10x objective) were 35 μW and 20 μW for the eGFP and mCherry excitation lasers, respectively. Three Hybrid Detectors (HyD) were used to acquire the fluorescent signal, with spectral windows of 496-546 nm, 600-660 nm, and 700-800 nm for the eGFP, mCherry, and iRFP signals, respectively. The confocal stack consisted of 15 equidistant slices with an overall z-height of 7 μm and an inter-slice distance of 0.5 μm. The images were acquired at a time resolution of 15 s, using an image resolution of 512 x 128 pixels, a pixel size of 202 nm, and a pixel dwell time of 1.2 μs. The signal from each frame was accumulated over 3 repetitions. Data were taken for 299 cells over a total of 7 embryos, and each embryo was imaged over the first 25 min of nuclear cycle 14.

Image analysis

Images were analyzed using custom-written software following the protocols in ***Garcia et al.*** (***2013***) and ***Lammers et al.*** (***2020***). Briefly, this procedure involved segmenting individual nuclei using the Histone-iRFP signal as a nuclear mask, segmenting each transcription spot based on its fluorescence, and calculating the intensity of each MCP-mCherry and PCP-eGFP transcription spot inside a nucleus as a function of time. The Trainable Weka Segmentation plugin for FIJI (***Arganda-Carreras et al., 2017***), which uses the FastRandomForest algorithm, was used to identify and segment the transcription spots.

Data Analysis

Inference was done using *MCMCstat*, an adaptive MCMC algorithm (***Haario et al., 2001***, ***2006***). Figures were generated using the open-source gramm package for MATLAB, developed by Pierre Morel (***Morel, 2018***). Generalized linear regression used in Fig. 3 utilized a normally distributed error model and was performed using MATLAB's *glmfit* function. All scripts relating to the MCMC inference method developed in this work are available at the associated GitHub repository.

Acknowledgements

We thank Sandeep Choubey, Antoine Coulon, Jane Kondev, Anders Sejr Hansen, Mustafa Mir, Rob Phillips, Manuel Razo-Mejia, and Matthew Ronshaugen for thoughtful comments on the manuscript. We also are grateful to Florian Jug, Nick Lammers, and Armando Reimer for their crucial work in developing the image analysis code used here.

This work was supported by the Burroughs Wellcome Fund Career Award at the Scientific Interface, the Sloan Research Foundation, the Human Frontiers Science Program, the Searle Scholars Program, the Shurl and Kay Curci Foundation, the Hellman Foundation, the NIH Director's New Innovator Award (DP2 OD024541-01), and an NSF CAREER Award (1652236) (HGG), an NSF GRFP (DGE 1752814) (EE, MT), a UC Berkeley Chancellor's Fellowship (EE), a KFAS scholarship (YJK), and an DoD NDSEG graduate fellowship (JL).

References

Alberts B. Molecular biology of the cell. Sixth edition. ed. New York, NY: Garland Science, Taylor and Francis Group; 2015.

Ali MZ, Choubey S, Das D, Brewster RC. Probing Mechanisms of Transcription Elongation Through Cell-to-Cell Variability of RNA Polymerase. Biophysical Journal. 2020; 118(7):1769–1781. https://doi.org/10.1016/j.bpj.2020.02.002, doi: 10.1016/j.bpj.2020.02.002.

Ardehali MB, Lis JT. Tracking rates of transcription and splicing in vivo. Nat Struct Mol Biol. 2009; 16(11):1123–4. doi: 10.1038/nsmb1109-1123.

Arganda-Carreras I, Kaynig V, Rueden C, Eliceiri KW, Schindelin J, Cardona A, Seung HS. Trainable Weka Segmentation: A machine learning tool for microscopy pixel classification. Bioinformatics. 2017; 33(15):2424–2426. doi: 10.1093/bioinformatics/btx180.

Bai L, Santangelo TJ, Wang MD. Single-molecule analysis of RNA polymerase transcription. Annual Review of Biophysics and Biomolecular Structure. 2006; 35:343–360. doi: 10.1146/annurev.biophys.35.010406.150153.

Bakker E, Swain PS. Estimating numbers of intracellular molecules through analysing fluctuations in photo-bleaching. Sci Rep. 2019; 9(1):15238. doi: 10.1038/s41598-019-50921-7.

Bartman CR, Hsu SC, Hsiung CC, Raj A, Blobel GA. Enhancer Regulation of Transcriptional Bursting Parameters Revealed by Forced Chromatin Looping. Mol Cell. 2016; 62(2):237–247. doi: 10.1016/j.molcel.2016.03.007.

Batsché E, Yaniv M, Muchardt C. The human SWI/SNF subunit Brm is a regulator of alternative splicing. Nature Structural and Molecular Biology. 2006; 13(1):22–29. doi: 10.1038/nsmb1030.

Bentley DL. Coupling mRNA processing with transcription in time and space. Nat Rev Genet. 2014; 15(3):163–75. doi: 10.1038/nrg3662.

Bertrand E, Chartrand P, Schaefer M, Shenoy SM, Singer RH, Long RM. Localization of ASH1 mRNA particles in living yeast. Mol Cell. 1998; 2(4):437–45. doi: S1097-2765(00)80143-4 [pii].

Boettiger AN, Levine M. Rapid transcription fosters coordinate snail expression in the Drosophila embryo. Cell Rep. 2013; 3(1):8–15. doi: 10.1016/j.celrep.2012.12.015.

Boettiger AN, Ralph PL, Evans SN. Transcriptional Regulation: Effects of Promoter Proximal Pausing on Speed, Synchrony and Reliability. PLoS Computational Biology. 2011; 7(5). doi: 10.1371/journal.pcbi.1001136.

Boireau S, Maiuri P, Basyuk E, de la Mata M, Knezevich A, Pradet-Balade B, Backer V, Kornblihtt A, Marcello A, Bertrand E. The transcriptional cycle of HIV-1 in real-time and live cells. J Cell Biol. 2007; 179(2):291–304. doi: 10.1083/jcb.200706018.

Bothma JP, Garcia HG, Esposito E, Schlissel G, Gregor T, Levine M. Dynamic regulation of eve stripe 2 expression reveals transcriptional bursts in living Drosophila embryos. Proc Natl Acad Sci U S A. 2014; 111(29):10598–10603. doi: 10.1073/pnas.1410022111.

Brewster RC, Weinert FM, Garcia HG, Song D, Rydenfelt M, Phillips R. The transcription factor titration effect dictates level of gene expression. Cell. 2014; 156(6):1312–23. doi: 10.1016/j.cell.2014.02.022.

Cai L, Friedman N, Xie XS. Stochastic protein expression in individual cells at the single molecule level. Nature. 2006; 440(7082):358–62.

Carrillo Oesterreich F, Preibisch S, Neugebauer KM. Global analysis of nascent rna reveals transcriptional pausing in terminal exons. Molecular Cell. 2010; 40(4):571–581. http://dx.doi.org/10.1016/j.molcel.2010.11.004, doi: 10.1016/j.molcel.2010.11.004.

Chao JA, Patskovsky Y, Almo SC, Singer RH. Structural basis for the coevolution of a viral RNA-protein complex. Nat Struct Mol Biol. 2008; 15(1):103–5. doi: nsmb1327 [pii] 10.1038/nsmb1327.

Chen H, Levo M, Barinov L, Fujioka M, Jaynes JB, Gregor T. Dynamic interplay between enhancer-promoter topology and gene activity. Nat Genet. 2018; 50(9):1296–1303. doi: 10.1038/s41588-018-0175-z.

Chen H, Xu Z, Mei C, Yu D, Small S. A system of repressor gradients spatially organizes the boundaries of bicoid-dependent target genes. Cell. 2012; 149(3):618–29. doi: 10.1016/j.cell.2012.03.018.

Choubey S, Kondev J, Sanchez A. Deciphering Transcriptional Dynamics In Vivo by Counting Nascent RNA Molecules. PLoS Comput Biol. 2015; 11(11):e1004345. doi: 10.1371/journal.pcbi.1004345.

Choubey S, Kondev J, Sanchez A. Distribution of Initiation Times Reveals Mechanisms of Transcriptional Regulation in Single Cells. Biophysical Journal. 2018; 114(9):2072–2082. http://linkinghub.elsevier.com/retrieve/pii/S0006349518304077, doi: 10.1016/j.bpj.2018.03.031.

Chubb JR, Trcek T, Shenoy SM, Singer RH. Transcriptional pulsing of a developmental gene. Curr Biol. 2006; 16(10):1018–25. doi: S0960-9822(06)01426-6 [pii] 10.1016/j.cub.2006.03.092.

Churchman LS, Weissman JS. Nascent transcript sequencing visualizes transcription at nucleotide resolution. Nature. 2011; 469(7330):368–+. doi: Doi 10.1038/Nature09652.

Combs PA, Eisen MB. Genome-wide measurement of spatial expression in patterning mutants of Drosophila melanogaster. F1000Res. 2017; 6:41. doi: 10.12688/f1000research.9720.1.

Core LJ, Waterfall JJ, Lis JT. Nascent RNA sequencing reveals widespread pausing and divergent initiation at human promoters. Science. 2008; 322(5909):1845–1848. doi: 10.1126/science.1162228.

Corrigan AM, Tunnacliffe E, Cannon D, Chubb JR. A continuum model of transcriptional bursting. Elife. 2016; 5. doi: 10.7554/eLife.13051.

Corrigan AM, Chubb JR. Regulation of transcriptional bursting by a naturally oscillating signal. Current Biology. 2014; 24(2):205–211. http://dx.doi.org/10.1016/j.cub.2013.12.011, doi: 10.1016/j.cub.2013.12.011.

Coulon A, Chow CC, Singer RH, Larson DR. Eukaryotic transcriptional dynamics: from single molecules to cell populations. Nat Rev Genet. 2013; 14(8):572–84. doi: 10.1038/nrg3484.

Coulon A, Ferguson ML, de Turris V, Palangat M, Chow CC, Larson DR. Kinetic competition during the transcription cycle results in stochastic RNA processing. Elife. 2014; 3. doi: 10.7554/eLife.03939.

Danko CG, Hah N, Luo X, Martins AL, Core L, Lis JT, Siepel A, Kraus WL. Signaling Pathways Differentially Affect RNA Polymerase II Initiation, Pausing, and Elongation Rate in Cells. Molecular Cell. 2013; 50(2):212–222. doi: 10.1016/j.molcel.2013.02.015.

Darzacq X, Shav-Tal Y, de Turris V, Brody Y, Shenoy SM, Phair RD, Singer RH. In vivo dynamics of RNA polymerase II transcription. Nat Struct Mol Biol. 2007; 14(9):796–806. doi: 10.1038/nsmb1280.

De La Mata M, Alonso CR, Kadener S, Fededa JP, Blaustein M, Pelisch F, Cramer P, Bentley D, Kornblihtt AR. A slow RNA polymerase II affects alternative splicing in vivo. Molecular Cell. 2003; 12(2):525–532. doi: 10.1016/j.molcel.2003.08.001.

Desponds J, Tran H, Ferraro T, Lucas T, Perez Romero C, Guillou A, Fradin C, Coppey M, Dostatni N, Walczak AM. Precision of Readout at the hunchback Gene: Analyzing Short Transcription Time Traces in Living Fly Embryos. PLoS Comput Biol. 2016; 12(12):e1005256. doi: 10.1371/journal.pcbi.1005256.

Driever W, Nusslein-Volhard C. The bicoid protein is a positive regulator of hunchback transcription in the early Drosophila embryo. Nature. 1989; 337(6203):138–43. doi: 10.1038/337138a0.

Dufourt J, Trullo A, Hunter J, Fernandez C, Lazaro J, Dejean M, Morales L, Nait-Amer S, Schulz KN, Harrison MM, Favard C, Radulescu O, Lagha M. Temporal control of gene expression by the pioneer factor Zelda through transient interactions in hubs. Nat Commun. 2018; 9(1):5194. doi: 10.1038/s41467-018-07613-z.

Eck E, Liu J, Kazemzadeh-Atoufi M, Ghoreishi S, Blythe SA, Garcia H. Quantitative dissection of transcription in development yields evidence for transcription factor-driven chromatin accessibility. bioRxiv. 2020; p. 2020.01.27.922054. doi: 10.1101/2020.01.27.922054.

Elowitz MB, Levine AJ, Siggia ED, Swain PS. Stochastic gene expression in a single cell. Science. 2002; 297(5584):1183–6.

Falo-Sanjuan J, Lammers NC, Garcia HG, Bray SJ. Enhancer Priming Enables Fast and Sustained Transcriptional Responses to Notch Signaling. Dev Cell. 2019; 50(4):411–425 e8. doi: 10.1016/j.devcel.2019.07.002.

Femino AM, Fay FS, Fogarty K, Singer RH. Visualization of single RNA transcripts in situ. Science. 1998; 280(5363):585–90.

Ferraro T, Lucas T, Clemot M, De Las Heras Chanes J, Desponds J, Coppey M, Walczak AM, Dostatni N. New methods to image transcription in living fly embryos: the insights so far, and the prospects. Wiley Interdiscip Rev Dev Biol. 2016; 5(3):296–310. doi: 10.1002/wdev.221.

Fong N, Brannan K, Erickson B, Kim H, Cortazar MA, Sheridan RM, Nguyen T, Karp S, Bentley DL. Effects of Transcription Elongation Rate and Xrn2 Exonuclease Activity on RNA Polymerase II Termination Suggest Widespread Kinetic Competition. Molecular Cell. 2015; 60(2):256–267. doi: 10.1016/j.molcel.2015.09.026.

Fritzsch C, Baumgartner S, Kuban M, Steinshorn D, Reid G, Legewie S. Estrogen-dependent control and cell-to-cell variability of transcriptional bursting. Mol Syst Biol. 2018; 14(2):e7678. doi: 10.15252/msb.20177678.

Fuchs G, Voichek Y, Benjamin S, Shlomit G, Amit I, Moshe O. 4sUDRB-seq: measuring genomewide transcriptional elongation rates and initiation frequencies within cells. Genome Biology. 2014; 15(5):R69. doi: 10.1186/gb-2014-15-5-r69.

Fuda NJ, Ardehali MB, Lis JT. Defining mechanisms that regulate RNA polymerase II transcription in vivo. Nature. 2009; 461(7261):186–92. doi: 10.1038/nature08449.

Fukaya T, Lim B, Levine M. Enhancer Control of Transcriptional Bursting. Cell. 2016; 166(2):358–368. doi: 10.1016/j.cell.2016.05.025.

Fukaya T, Lim B, Levine M. Rapid Rates of Pol II Elongation in the Drosophila Embryo. Curr Biol. 2017; 27(9):1387–1391. doi: 10.1016/j.cub.2017.03.069.

Garcia HG, Tikhonov M, Lin A, Gregor T. Quantitative imaging of transcription in living Drosophila embryos links polymerase activity to patterning. Curr Biol. 2013; 23(21):2140–5. doi: 10.1016/j.cub.2013.08.054.

Garcia HG, Gregor T. In: Gaspar I, editor. Live Imaging of mRNA Synthesis in Drosophila New York, NY: Springer New York; 2018. p. 349–357.

Geyer CJ. Practical Markov Chain Monte Carlo. Statistical Science. 1992; 7(4):473–483. doi: 10.1097/EDE.0b013e3181.

Golding I, Paulsson J, Zawilski SM, Cox EC. Real-time kinetics of gene activity in individual bacteria. Cell. 2005; 123(6):1025–36.

Gorski SA, Dundr M, Misteli T. The road much traveled: trafficking in the cell nucleus. Current Opinion in Cell Biology. 2006; 18(3):284–290. doi: 10.1016/j.ceb.2006.03.002.

Haario H, Laine M, Mira A, Saksman E. DRAM: Efficient adaptive MCMC. Statistics and Computing. 2006; 16(4):339–354. doi: 10.1007/s11222-006-9438-0.

Haario H, Saksman E, Tamminen J. An Adaptive Metropolis Algorithm. Bernoulli. 2001; 7(2):223. http://www.jstor.org/stable/3318737?origin=crossref, doi: 10.2307/3318737.

Haines JE, Eisen MB. Patterns of chromatin accessibility along the anterior-posterior axis in the early Drosophila embryo. PLoS Genet. 2018; 14(5):e1007367. doi: 10.1371/journal.pgen.1007367.

Hampsey M, Singh BN, Ansari A, Lainé JP, Krishnamurthy S. Control of eukaryotic gene expression: Gene loops and transcriptional memory. Advances in Enzyme Regulation. 2011; 51(1):118–125. http://dx.doi.org/10.1016/j.advenzreg.2010.10.001, doi: 10.1016/j.advenzreg.2010.10.001.

Hazelbaker DZ, Marquardt S, Wlotzka W, Buratowski S. Kinetic Competition between RNA Polymerase II and Sen1-Dependent Transcription Termination. Molecular Cell. 2013; doi: 10.1016/j.molcel.2012.10.014.

Hendy O, Campbell J J, Weissman JD, Larson DR, Singer DS. Differential context-specific impact of individual core promoter elements on transcriptional dynamics. Mol Biol Cell. 2017; 28(23):3360–3370. doi: 10.1091/mbc.E17-06-0408.

Herbert KM, Greenleaf WJ, Block SM. Single-Molecule Studies of RNA Polymerase: Motoring Along. Annual Review of Biochemistry. 2008; 77(1):149–176. doi: 10.1146/annurev.biochem.77.073106.100741.

Hocine S, Raymond P, Zenklusen D, Chao JA, Singer RH. Single-molecule analysis of gene expression using two-color RNA labeling in live yeast. Nature Methods. 2013; 10(2):119–121. doi: 10.1038/nmeth.2305.

Jones DL, Brewster RC, Phillips R. Promoter architecture dictates cell-to-cell variability in gene expression. Science. 2014; 346(6216):1533–6. doi: 10.1126/science.1255301.

Jonkers I, Lis JT. Getting up to speed with transcription elongation by RNA polymerase II. Nature Reviews Molecular Cell Biology. 2015; 16(3):167–177. doi: 10.1038/nrm3953.

Jung W, Tschaplinski T, Wang L, Glazebrook J, Greenberg J. Priming in systemic plant immunity. Science. 2009; 324(5923):89–91. https://www.sciencemagazinedigital.org/sciencemagazine/22{_}june{_}2018/MobilePagedArticle.action?articleId=1404350{&}app=false{#}articleId1404350, doi: 10.1126/science.

Kim NH, Lee G, Sherer NA, Martini KM, Goldenfeld N, Kuhlman TE. Real-time transposable element activity in individual live cells. Proc Natl Acad Sci U S A. 2016; 113(26):7278–83. doi: 10.1073/pnas.1601833113.

Klumpp S. Pausing and Backtracking in Transcription Under Dense Traffic Conditions. Journal of Statistical Physics. 2011; 142(6):1252–1267. doi: 10.1007/s10955-011-0120-3.

Klumpp S, Hwa T. Stochasticity and traffic jams in the transcription of ribosomal RNA: Intriguing role of termination and antitermination. Proceedings of the National Academy of Sciences of the United States of America. 2008; 105(47):18159–18164. doi: 10.1073/pnas.0806084105.

Kuehner JN, Pearson EL, Moore C. Unravelling the means to an end: RNA polymerase II transcription termination. Nature Reviews Molecular Cell Biology. 2011; 12(5):283–294. http://dx.doi.org/10.1038/nrm3098, doi: 10.1038/nrm3098.

Lammers NC, Galstyan V, Reimer A, Medin SA, Wiggins CH, Garcia HG. Multimodal transcriptional control of pattern formation in embryonic development. Proc Natl Acad Sci U S A. 2020; 117(2):836–847. doi: 10.1073/pnas.1912500117.

Larschan E, Bishop EP, Kharchenko PV, Core LJ, Lis JT, Park PJ, Kuroda MI. X chromosome dosage compensation via enhanced transcriptional elongation in Drosophila. Nature. 2011; 471(7336):115–8. doi: 10.1038/nature09757.

Larson DR, Singer RH, Zenklusen D. A single molecule view of gene expression. Trends Cell Biol. 2009; 19(11):630–7. doi: S0962-8924(09)00188-3 [pii] 10.1016/j.tcb.2009.08.008.

Larson DR, Zenklusen D, Wu B, Chao JA, Singer RH. Real-time observation of transcription initiation and elongation on an endogenous yeast gene. Science. 2011; 332(6028):475–8. doi: 332/6028/475 [pii] 10.1126/science.1202142.

Larson MH, Landick R, Block SM. Single-Molecule Studies of RNA Polymerase: One Singular Sensation, Every Little Step It Takes. Molecular Cell. 2011; 41(3):249–262. http://dx.doi.org/10.1016/j.molcel.2011.01.008, doi: 10.1016/j.molcel.2011.01.008.

Lee C, Shin H, Kimble J. Dynamics of Notch-Dependent Transcriptional Bursting in Its Native Context. Dev Cell. 2019; 50(4):426–435 e4. doi: 10.1016/j.devcel.2019.07.001.

Lenstra TL, Rodriguez J, Chen H, Larson DR. Transcription Dynamics in Living Cells. Annual Review of Biophysics. 2016; 45(1):25–47. doi: 10.1146/annurev-biophys-062215-010838.

Li J, Dong A, Saydaminova K, Chang H, Wang G, Ochiai H, Yamamoto T, Pertsinidis A. Single-Molecule Nanoscopy Elucidates RNA Polymerase II Transcription at Single Genes in Live Cells. Cell. 2019; doi: 10.1016/j.cell.2019.05.029.

Little SC, Tikhonov M, Gregor T. Precise developmental gene expression arises from globally stochastic transcriptional activity. Cell. 2013; 154(4):789–800. doi: 10.1016/j.cell.2013.07.025.

Liu X, Freitas J, Zheng D, Oliveira MS, Hoque M, Martins T, Henriques T, Tian B, Moreira A. Transcription elongation rate has a tissue-specific impact on alternative cleavage and polyadenylation in Drosophila melanogaster. Rna. 2017; 23(12):1807–1816. doi: 10.1261/rna.062661.117.

Lucas T, Ferraro T, Roelens B, De Las Heras Chanes J, Walczak AM, Coppey M, Dostatni N. Live imaging of bicoid-dependent transcription in Drosophila embryos. Curr Biol. 2013; 23(21):2135–9. doi: 10.1016/j.cub.2013.08.053.

Lucas T, Tran H, Perez Romero CA, Guillou A, Fradin C, Coppey M, Walczak AM, Dostatni N. 3 minutes to precisely measure morphogen concentration. PLoS Genet. 2018; 14(10):e1007676. doi: 10.1371/journal.pgen.1007676.

Luria SE, Delbruck M. Mutations of Bacteria from Virus Sensitivity to Virus Resistance. Genetics. 1943; 28(6):491–511.

Mapendano CK, Lykke-Andersen S, Kjems J, Bertrand E, Jensen TH. Crosstalk between mRNA 3 End Processing and Transcription Initiation. Molecular Cell. 2010; 40(3):410–422. doi: 10.1016/j.molcel.2010.10.012.

Margolis JS, Borowsky ML, Steingrimsson E, Shim CW, Lengyel JA, Posakony JW. Posterior stripe expression of hunchback is driven from two promoters by a common enhancer element. Development. 1995; 121(9):3067–77.

Moore MJ, Proudfoot NJ. Pre-mRNA Processing Reaches Back toTranscription and Ahead to Translation. Cell. 2009; 136(4):688–700. http://dx.doi.org/10.1016/j.cell.2009.02.001, doi: 10.1016/j.cell.2009.02.001.

Morel P. Gramm: grammar of graphics plotting in Matlab. The Journal of Open Source Software. 2018; 3(23):568. doi: 10.21105/joss.00568.

Muramoto T, Cannon D, Gierlinski M, Corrigan A, Barton GJ, Chubb JR. Live imaging of nascent RNA dynamics reveals distinct types of transcriptional pulse regulation. Proc Natl Acad Sci U S A. 2012; doi: 1117603109 [pii] 10.1073/pnas.1117603109.

Muse GW, Gilchrist DA, Nechaev S, Shah R, Parker JS, Grissom SF, Zeitlinger J, Adelman K. RNA polymerase is poised for activation across the genome. Nature Genetics. 2007; 39(12):1507–1511. doi: 10.1038/ng.2007.21.

Padovan-Merhar O, Nair GP, Biaesch AG, Mayer A, Scarfone S, Foley SW, Wu AR, Churchman LS, Singh A, Raj A. Single mammalian cells compensate for differences in cellular volume and DNA copy number through independent global transcriptional mechanisms. Mol Cell. 2015; 58(2):339–52. doi: 10.1016/j.molcel.2015.03.005.

Paige JS, Wu KY, Jaffrey SR. RNA Mimics of Green Fluorescent Protein. Science. 2011; 333(July). doi: 10.1126/science.1207339.

Palangat M, Larson DR. Complexity of RNA polymerase II elongation dynamics. Biochimica et Biophysica Acta - Gene Regulatory Mechanisms. 2012; 1819(7):667–672. http://dx.doi.org/10.1016/j.bbagrm.2012.02.024, doi: 10.1016/j.bbagrm.2012.02.024.

Pare A, Lemons D, Kosman D, Beaver W, Freund Y, McGinnis W. Visualization of individual Scr mRNAs during Drosophila embryogenesis yields evidence for transcriptional bursting. Curr Biol. 2009; 19(23):2037–42. doi: S0960-9822(09)01848-X [pii] 10.1016/j.cub.2009.10.028.

Perry MW, Bothma JP, Luu RD, Levine M. Precision of hunchback expression in the Drosophila embryo. Curr Biol. 2012; 22(23):2247–52. doi: 10.1016/j.cub.2012.09.051.

Pinto PAB, Henriques T, Freitas MO, Martins T, Domingues RG, Wyrzykowska PS, Coelho PA, Carmo AM, Sunkel CE, Proudfoot NJ, Moreira A. RNA polymerase II kinetics in polo polyadenylation signal selection. EMBO Journal. 2011; 30(12):2431–2444. doi: 10.1038/emboj.2011.156.

Raj A, Peskin CS, Tranchina D, Vargas DY, Tyagi S. Stochastic mRNA synthesis in mammalian cells. PLoS Biol. 2006; 4(10):e309. doi: 06-PLBI-RA-0625R2 [pii] 10.1371/journal.pbio.0040309.

Raser JM, O'Shea EK. Control of stochasticity in eukaryotic gene expression. Science. 2004; 304(5678):1811–4.

Richard P, Manley JL. Transcription termination by nuclear RNA polymerases. Genes Dev. 2009; 23(11):1247–69. doi: 10.1101/gad.1792809.

Rodriguez J, Larson DR. Transcription in Living Cells: Molecular Mechanisms of Bursting. Annu Rev Biochem. 2020; 89:189–212. doi: 10.1146/annurev-biochem-011520-105250.

Roeder RG. The complexities of eukaryotic transcription initiation: regulation of preinitiation complex assembly. Trends in Biochemical Sciences. 1991; 16:402–408.

Rosenfeld N, Perkins TJ, Alon U, Elowitz MB, Swain PS. A fluctuation method to quantify in vivo fluorescence data. Biophys J. 2006; 91(2):759–66. doi: S0006-3495(06)71774-X [pii] 10.1529/biophysj.105.073098.

Rosenfeld N, Young JW, Alon U, Swain PS, Elowitz MB. Gene regulation at the single-cell level. Science. 2005; 307(5717):1962–5.

Sanchez A, Choubey S, Kondev J. Regulation of noise in gene expression. Annu Rev Biophys. 2013; 42:469–91. doi: 10.1146/annurev-biophys-083012-130401.

Sanchez A, Garcia HG, Jones D, Phillips R, Kondev J. Effect of Promoter Architecture on the Cell-to-Cell Variability in Gene Expression. PLoS Comput Biol. 2011; 7(3):e1001100. doi: 10.1371/journal.pcbi.1001100.

Sanchez A, Golding I. Genetic determinants and cellular constraints in noisy gene expression. Science. 2013; 342(6163):1188–93. doi: 10.1126/science.1242975.

Sato H, Das S, Singer RH, Vera M. Imaging of DNA and RNA in Living Eukaryotic Cells to Reveal Spatiotemporal Dynamics of Gene Expression. Annual review of biochemistry. 2020; p. 1–29. http://www.ncbi.nlm.nih.gov/pubmed/32176523, doi: 10.1146/annurev-biochem-011520-104955.

Saunders A, Core LJ, Lis JT. Breaking barriers to transcription elongation. Nature Reviews Molecular Cell Biology. 2006; 7(8):557–567. doi: 10.1038/nrm1981.

Selby CP, Drapkin R, Reinberg D, Sancar A. RNA polymerase II stalled at a thymine dimer: Footprint and effect on excision repair. Nucleic Acids Research. 1997; 25(4):787–793. doi: 10.1093/nar/25.4.787.

Senecal A, Munsky B, Proux F, Ly N, Braye FE, Zimmer C, Mueller F, Darzacq X. Transcription factors modulate c-Fos transcriptional bursts. Cell Rep. 2014; 8(1):75–83. doi: 10.1016/j.celrep.2014.05.053.

Serov AS, Levine AJ, Mani M. Abortive Initiation as a Bottleneck for Transcription in the Early Drosophila Embryo. ArXiv e-prints. 2017; p. 1701.06079.

Skinner SO, Xu H, Nagarkar-Jaiswal S, Freire PR, Zwaka TP, Golding I. Single-cell analysis of transcription kinetics across the cell cycle. Elife. 2016; 5:e12175. doi: 10.7554/eLife.12175.

So LH, Ghosh A, Zong C, Sepulveda LA, Segev R, Golding I. General properties of transcriptional time series in Escherichia coli. Nat Genet. 2011; 43(6):554–60. doi: 10.1038/ng.821.

Spitz F, Furlong EE. Transcription factors: from enhancer binding to developmental control. Nat Rev Genet. 2012; 13(9):613–26. doi: 10.1038/nrg3207.

Tantale K, Mueller F, Kozulic-Pirher A, Lesne A, Victor JM, Robert MC, Capozi S, Chouaib R, Backer V, Mateos-Langerak J, Darzacq X, Zimmer C, Basyuk E, Bertrand E. A single-molecule view of transcription reveals convoys of RNA polymerases and multi-scale bursting. Nat Commun. 2016; 7:12248. doi: 10.1038/ncomms12248.

Teng SW, Wang Y, Tu KC, Long T, Mehta P, Wingreen NS, Bassler BL, Ong NP. Measurement of the copy number of the master quorum-sensing regulator of a bacterial cell. Biophys J. 2010; 98(9):2024–31. doi: S0006-3495(10)00175-X [pii] 10.1016/j.bpj.2010.01.031.

Tian B, Manley JL. Alternative polyadenylation of mRNA precursors. Nature Reviews Molecular Cell Biology. 2016; 18(1):18–30. http://dx.doi.org/10.1038/nrm.2016.116, doi: 10.1038/nrm.2016.116.

Tolić-Nørrelykke SF, Engh AM, Landick R, Gelles J. Diversity in the Rates of Transcript Elongation by Single RNA Polymerase Molecules. Journal of Biological Chemistry. 2004; 279(5):3292–3299. doi: 10.1074/jbc.M310290200.

Wu B, Chen J, Singer RH. Background free imaging of single mRNAs in live cells using split fluorescent proteins. Sci Rep. 2014; 4:3615. doi: 10.1038/srep03615.

Wu B, Eliscovich C, Yoon YJ, Singer RH. Translation dynamics of single mRNAs in live cells and neurons. Science. 2016; 352(6292):1430–5. doi: 10.1126/science.aaf1084.

Xu H, Sepulveda LA, Figard L, Sokac AM, Golding I. Combining protein and mRNA quantification to decipher transcriptional regulation. Nat Methods. 2015; 12(8):739–42. doi: 10.1038/nmeth.3446.

Zenklusen D, Larson DR, Singer RH. Single-RNA counting reveals alternative modes of gene expression in yeast. Nat Struct Mol Biol. 2008; 15(12):1263–71. doi: nsmb.1514 [pii] 10.1038/nsmb.1514.

Zoller B, Little SC, Gregor T. Diverse Spatial Expression Patterns Emerge from Unified Kinetics of Transcriptional Bursting. Cell. 2018; 175(3):835–847 e25. doi: 10.1016/j.cell.2018.09.056.

Supplementary Information

S1 Full Model

To predict MS2 and PP7 fluorescence traces, we utilized a simple model of transcription initiation, elongation, and cleavage. The entire model has the following free parameters:

- $\langle R \rangle$, the mean transcription initiation rate
- $\delta R(t)$, the time-dependent fluctuations in the transcription initiation rate around the mean $\langle R \rangle$
- v_{elon}, the RNAP elongation rate
- τ_{cleave}, the mRNA cleavage time
- t_{on}, the time of transcription onset after the previous mitosis, where $t = 0$ corresponds to the start of anaphase.
- MS2_{basal}, the basal level of MCP-mCherry fluorescence
- PP7_{basal}, the basal level of PCP-eGFP fluorescence
- α, the scaling factor between MCP-mCherry and PCP-eGFP arbitrary fluorescence units (see Section S4 for more details)

First, the parameters $\langle R \rangle$, $\delta R(t)$, t_{on}, v_{elon}, and τ_{cleave} were used to generate a map $x_i(t)$ of the position of each actively transcribing RNAP molecule i along the body of the reporter gene, as a function of time. Given a computational time step dt, $R(t)dt$ RNAP molecules are loaded at time point t at the promoter $x = 0$, where

$$R(t) = \begin{cases} 0 & t < t_{on} \\ \langle R \rangle + \delta R(t) & t \geq t_{on}. \end{cases} \tag{S1}$$

After initiation, each RNAP molecule then proceeds forward with the constant elongation rate v_{elon}. Once an RNAP molecule reaches the end of the gene, an additional cleavage time τ_{cleave} elapses, after which the nascent transcript is cleaved and disappears instantly. This assumption of instantaneous disappearance following cleavage is justified in Section S2 based on the diffusion time scale of individual mRNA molecules.

From this position map, and based on the locations of the stem loop sequences along the reporter construct (Fig. S1A), we calculate the predicted MS2 and PP7 fluorescence signals. the contribution to the MS2 signal $F_i^{MS2}(t)$ of an individual RNAP molecule i at position $x_i(t)$ is given by

$$F_i^{MS2}(t) = \begin{cases} 0 & x_i(t) < x_{MS2}^{start} \\ \frac{x_i(t) - x_{MS2}^{start}}{x_{MS2}^{end} - x_{MS2}^{start}} F_{MS2} & x_{MS2}^{start} \leq x_i(t) < x_{MS2}^{end} \\ F_{MS2} & x_i(t) \geq x_{MS2}^{end} \end{cases}, \tag{S2}$$

where x_{MS2}^{start} and x_{MS2}^{end} are the start and end positions of the MS2 stem loop sequence, respectively, and F_{MS2} is the mCherry fluorescence produced by a single RNAP molecule that has transcribed the entire set of MS2 stem loops. Here, we also assume that RNAP molecules that have only partially transcribed the MS2 stem loops result in a fractional fluorescence given by the fractional length of the MS2 stem loop sequence transcribed. Similarly, the contribution to the PP7 signal $F_i^{PP7}(t)$ is given by

$$F_i^{PP7}(t) = \begin{cases} 0 & x_i(t) < x_{PP7}^{start} \\ \frac{x_i(t) - x_{PP7}^{start}}{x_{PP7}^{end} - x_{PP7}^{start}} F_{PP7} & x_{PP7}^{start} \leq x_i(t) < x_{PP7}^{end} \\ F_{PP7} & x_i(t) \geq x_{PP7}^{end} \end{cases}, \tag{S3}$$

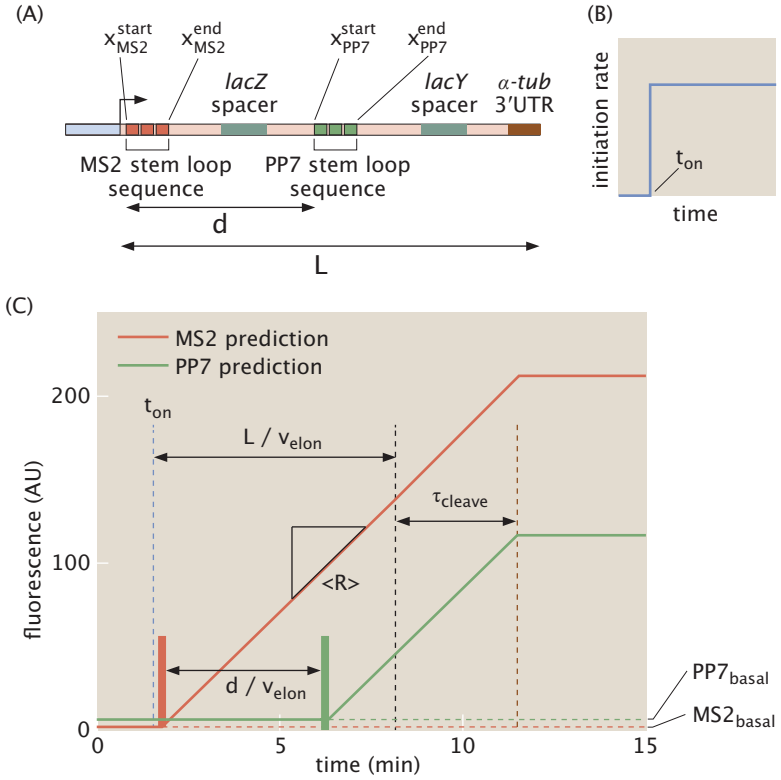

Figure S1. Detailed description of reporter construct and model used throughout this work. (A) Graphical map of the reporter construct used in this work. Labeled positions are $x^{start}_{MS2} = 0.024$ kb, $x^{end}_{MS2} = 1.299$ kb, $x^{start}_{PP7} = 4.292$ kb, and $x^{end}_{PP7} = 5.758$ kb, where $x = 0$ corresponds to the 3' end of the promoter. Distances are $d = 4.27$ kb and $L = 6.63$ kb. (B) Idealized scenario with a step of initiation rate that starts at zero and switches to magnitude $< R >$ at time $t = t_{on}$. (C) Relationship between fluorescence trace profiles and model parameters for the scenario in (B). Here, the two fluorescence traces are already rescaled by α to be in the same arbitrary units – see Section S4 for how this is achieved.

where x_{PP7}^{start} and x_{PP7}^{end} are the start and end positions of the PP7 stem loop sequence, respectively, and F_{PP7} is the GFP fluorescence produced by a single RNAP molecule that has transcribed the entire set of PP7 stem loops.

The temporal dynamics of the total MS2 and PP7 signals $F_{MS2}(t)$ and $F_{PP7}(t)$ are then obtained by summing over all the individual RNAP molecule contributions for each timepoint

$$F_{MS2}(t) = \sum_{i=1}^{N} F_i^{MS2}(t) \tag{S4}$$

$$F_{PP7}(t) = \sum_{i=1}^{N} F_i^{PP7}(t), \tag{S5}$$

where i is the index of each individual RNAP molecule and N is the total number of loaded RNAP molecules. The final signal is then modified by accounting for the scaling factor α and the basal fluorescence values of MS2_{basal} and PP7_{basal}. α is necessary because the two fluorescent protein signals have different arbitrary units (see Section S4). Further, the two basal fluorescence values are incorporated to account for the experimentally observed low baseline fluorescence in each fluorescent channel. The final signals $F'_{MS2}(t)$ and $F'_{PP7}(t)$ are then given by

$$F'_{MS2}(t) = \begin{cases} \text{MS2}_{basal}/\alpha & F_{MS2}(t) < \text{MS2}_{basal} \\ F_{MS2}(t)/\alpha & F_{MS2}(t) \geq \text{MS2}_{basal} \end{cases} \tag{S6}$$

and

$$F'_{PP7}(t) = \begin{cases} \text{PP7}_{basal} & F_{PP7}(t) < \text{PP7}_{basal} \\ F_{PP7}(t) & F_{PP7}(t) \geq \text{PP7}_{basal}. \end{cases} \tag{S7}$$

All of the model parameters introduced in this section were used as free parameters in the fitting procedure described in Section S3.

Figure S1B and C show a qualitative description of how the various parameters influence the shape of the simulated MS2 and PP7 fluorescence traces. Here, we consider an idealized scenario where the initiation rate consists of a pulse that starts at zero and switches to a constant magnitude $< R >$ at time $t = t_{on}$ (Fig. S1B).

Figure S1C show the resulting simulated fluorescence values. As a baseline, the basal fluorescence of MS2 and PP7 cause both signals to always be nonzero (red and green horizontal dashed lines). Once the simulation time exceeds the value of t_{on} (blue dashed line), RNAP molecules begin initiating transcription at the promoter.

MS2 fluorescence (red curve) begins to rise once the first RNAP molecule reaches the start of the MS2 sequence (red vertical bar). The slope of the increase in MS2 fluorescence value is given by the mean initiation rate $\langle R \rangle$ (black triangle).

When the first RNAP molecule reaches the start of the PP7 sequence (green bar), the PP7 fluorescence also begins to rise with the same slope (green curve). The time between MS2 and PP7 signal onset is given by the distance d between the start of the two stem loop repeats divided by the elongation rate, v_{elon}.

After a time $\frac{L}{v_{elon}}$, where L is the total length of the reporter gene, the first RNAP molecule reaches the end of the gene (black dashed line). From here, after the cleavage time τ_{cleave} has elapsed (brown dashed line), nascent RNA transcripts begin cleaving and the two fluorescence signals plateau at a constant value.

S2 Justification for approximating transcript cleavage as instantaneous

In the model presented in Section S1, we assumed that, when a nascent RNA transcript is cleaved at the end of the reporter gene, its MS2 and PP7 fluorescence signals disappear instantaneously. Here, we justify this assumption by demonstrating that the timescale of mRNA diffusion away from the active locus is much shorter than the experimental resolution of our system.

When a nascent RNA transcript is cleaved, it diffuses away from the gene locus. For a free particle with diffusion coefficient D, the characteristic timescale τ to diffuse a length scale L is given by

$$\tau \sim \frac{L^2}{D}. \tag{S8}$$

In the context of the experiment performed here, this can interpreted as the timescale for a cleaved mRNA transcript to diffuse away from the diffraction-limited fluorescence punctum at the locus due to labeled nascent transcripts.

We can estimate the characteristic timescale τ by plugging in the following values. Assume that the completed transcript possesses a typical mRNA diffusion coefficient of $D \sim 0.1\ \mu m^2/s$ (***Gorski et al., 2006***). The length scale L corresponds to the Abbe diffraction limit, which yields $L \sim 250\ nm$ for green light with a wavelength of about $500\ nm$ and a microscope with a numerical aperture of 1. Plugging these values into the equation yields a diffusion time scale of

$$\tau \sim \frac{(250nm)^2}{0.1\mu m^2/s} \sim 0.625\ s. \tag{S9}$$

As a result, a newly cleaved mRNA transcript will typically diffuse away from the locus in less than a second, meaning that its MS2 and PP7 fluorescence signal will vanish much faster than the experimental time resolution of $15\ s$. For this reason, we can justify approximating the cleavage process as instantaneously removing the fluorescent signals of newly cleaved transcripts.

S3 MCMC Inference Procedure

S3.1 Overview and application of MCMC

The inference procedures described in the main text were carried out using the established technique of Markov Chain Monte Carlo (MCMC). Specifically, we used the MATLAB package MCMCstat, an adaptive MCMC technique (***Haario et al., 2001***, ***2006***). For detailed descriptions, we refer the reader to the the MCMCstat website (https://mjlaine.github.io/mcmcstat/), as well as to a technical overview of MCMC (***Geyer, 1992***). Briefly, MCMC allows for an estimation of the parameter values of a model that best fit the experimentally observed data along with an associated error. In this work, we use MCMC to infer the best fit values of the transcription cycle parameters given observed fluorescence data at the single-cell level. Then, we combine these inference results across cells to construct distributions of inferred values across the ensemble of cells.

MCMC calculates a Bayesian posterior probability distribution of each free parameter given the data by stochastically sampling different parameter values. For a given set of observations D and a model with parameters θ, the so-called posterior probability distribution of θ possessing a particular set of values is given by Bayes' theorem

$$\underbrace{p(\theta|D)}_{\text{posterior}} = \frac{\overbrace{p(D|\theta)}^{\text{likelihood}}\ \overbrace{p(\theta)}^{\text{prior}}}{\underbrace{p(D)}_{\text{evidence}}}. \tag{S10}$$

This posterior distribution is a combination of three components – the likelihood, prior, and evidence. This latter term represents the probability of the observations possessing their particular

values, and allows the overall posterior distribution to be normalized. In practice, the evidence term is often dropped since MCMC can still yield accurate results without requiring this normalization. Thus, we have

$$\underbrace{p(\theta|D)}_{\text{posterior}} \propto \overbrace{p(D|\theta)}^{\text{likelihood}} \overbrace{p(\theta)}^{\text{prior}}. \tag{S11}$$

The prior function contains *a priori* assumptions about the probability distribution of parameter values θ, and the likelihood function represents the probability of obtaining the observations, given a particular set of parameters θ. Thus, the *most likely* set of parameters θ occurs when the product of the likelihood and prior is maximized, resulting in a maximum in the posterior function. MCMC extends this by sampling different values of θ such that an approximation of the full posterior distribution is also obtained.

The prior distributions for the inferred parameters were set as follows. The prior distribution for the fluctuations in the initiation rate $\delta R(t)$ at each time point was assumed to be a Gaussian prior centered around 0 AU/min with a standard deviation of 30 AU/min. This penalized fluctuations that strayed too far from zero, smoothing the overall initiation rate $R(t)$. For the rest of the parameters, a uniform distribution was chosen using the following uniform intervals:

- v_{elon}: [0, 10] kb/min
- t_{on}: [0, 10] min
- α: [0, 1]
- τ_{cleave}: [0, 20] min
- MS2_{basal}: [0, 50] AU
- PP7_{basal}: [0, 50] AU
- $\langle R \rangle$: [0, 40] AU/min

For the likelihood function, a Gaussian error function was used

$$p(D|\theta) = e^{-SS}, \tag{S12}$$

where SS is a sum-of-squares residual function given by

$$SS = \sum_t (F_{data} - F_{prediction})^2. \tag{S13}$$

Here, the summation runs over individual time points, F_{data} corresponds to the MS2 or PP7 fluorescence at a given timepoint, and $F_{prediction}$ corresponds to the predicted MS2 or PP7 fluorescence according to the model, for a given set of parameter values. That is,

$$F_{data} = \left\{\text{MS2}_1, \ldots, \text{MS2}_N, \text{PP7}_1, \ldots \text{PP7}_N\right\} \tag{S14}$$

where the subscripts indicate the time index over N time points. Similarly,

$$F_{prediction} = \left\{\text{MS2}_1^{pred}, \ldots, \text{MS2}_N^{pred}, \text{PP7}_1^{pred}, \ldots \text{PP7}_N^{pred}\right\} \tag{S15}$$

where the superscripts indicate that these are model predictions evaluated at the experimental time points.

The MCMC approach samples values of parameters θ to approximate the posterior probability distribution. There are several algorithms that achieve this – the adaptive technique used in the MCMCstat package is an efficient algorithm that updates the sampling technique to more quickly arrive at the converged distribution.

For each inference run, an initial condition of parameter values is chosen. The algorithm then stochastically updates the next set of parameter values based on the current and previous values

of the posterior distribution function. After a preset number of updates (typically at least on the order of thousands), the algorithm stops, resulting in a *chain* of MCMC parameter value samples. The initial period following the initial condition, known as the *burn-in* time, is typically discarded since the results are not reliable. The remaining values of the chain comprise an approximation of the underlying posterior probability distribution, with smaller errors for longer run times.

For the purposes of this work, the MCMC procedure was run by separately inferring parameter values for the data corresponding to each single cell. For each inference, random parameter values were chosen for the initial condition of the sampling algorithm in order to prevent initial condition bias from affecting the inference results. The algorithm was run for a total of $20,000$ iterations, which, after removing a burn-in window of length $10,000$, resulted in a chain of length $10,000$ for each of the 299 cells examined. To assess whether or not the algorithm was run for a sufficient number of iterations, the final chain was examined for *rapid mixing*, where the sampled values of a particular parameter rapidly fluctuate around a converged value. Figure S2A highlights this rapid mixing in the inferred transcription cycle parameters of a sample single cell. The lack of long-timescale correlations, also exemplified by the quick decay of the autocorrelation function of each chain (Fig. S2B), indicates that the algorithm has converged. In addition, a corner plot of the three transcription cycle parameters (Fig. S2C) illustrates the pairwise correlations between them, demonstrating that the inference did not encounter degenerate solutions, and that each parameter has a fairly unimodal distribution.

These diagnostics provided a check on the quality of the inference results. Afterwards, the mean value of each parameter's final chain was then retained for each single cell for use in the further statistical analysis carried out in the main text.

S3.2 Hierarchical inference procedure

Naively running the MCMC inference on the entire 18 min window of time for each single cell's worth of data compromised the quality of the inferred elongation rate. This is highlighted in Figure S3A, which shows the results of running the MCMC procedure on the entire 18 min window of fluorescence data for sample data from a single cell. The fit deviates from the true MS2 and PP7 signals at early timepoints (black lines), resulting in an unreliable measure of the elongation rate. This deviation stems from the inference procedure treating each time point as equally important, whereas, in reality, earlier time points are more important for estimating the elongation rate since they capture the onset of the MS2 and PP7 fluorescence signals.

To resolve this problem, we split the inference procedure into a hierarchy, where we chose to first run the MCMC procedure on an initial subset of the whole time window, consisting of the first 10 min of fluorescent signal. This time window was long enough to capture the initial rise in both fluorescent channels, but neglected the later time points that did not matter as much for the estimation of the elongation rate. Figure S3B shows the best fit of the MCMC procedure run on only this initial period, where the fit better captures the onset of signal in both fluorescent channels. Comparing the overall inferred elongation rates using the short and long time windows indicated that the long time-window inference scheme yielded systematically lower and more variable single-cell elongation rate values, with a mean and standard deviation of 1.90 kb/min and 1.24 kb/min, respectively (Fig. S3D, purple). In contrast, the inference performed over the short time window yielded a more constrained distribution, with a mean and standard deviation of 1.84 kb/min and 0.75 kb/min, respectively (Fig. S3D, yellow).

We next we ran the MCMC procedure on the whole 18 min time window for each single cell, but fixed the value of the elongation rate, v_{elon}, to the best-fit value from the initial inference done previously for that same cell. This did not introduce significant error to the fit, as seen in Figure S3C. Instead, this hierarchical method simply biased earlier time points to be more important for the elongation rate in particular. Thus, with this scheme, we were able to establish a robust procedure

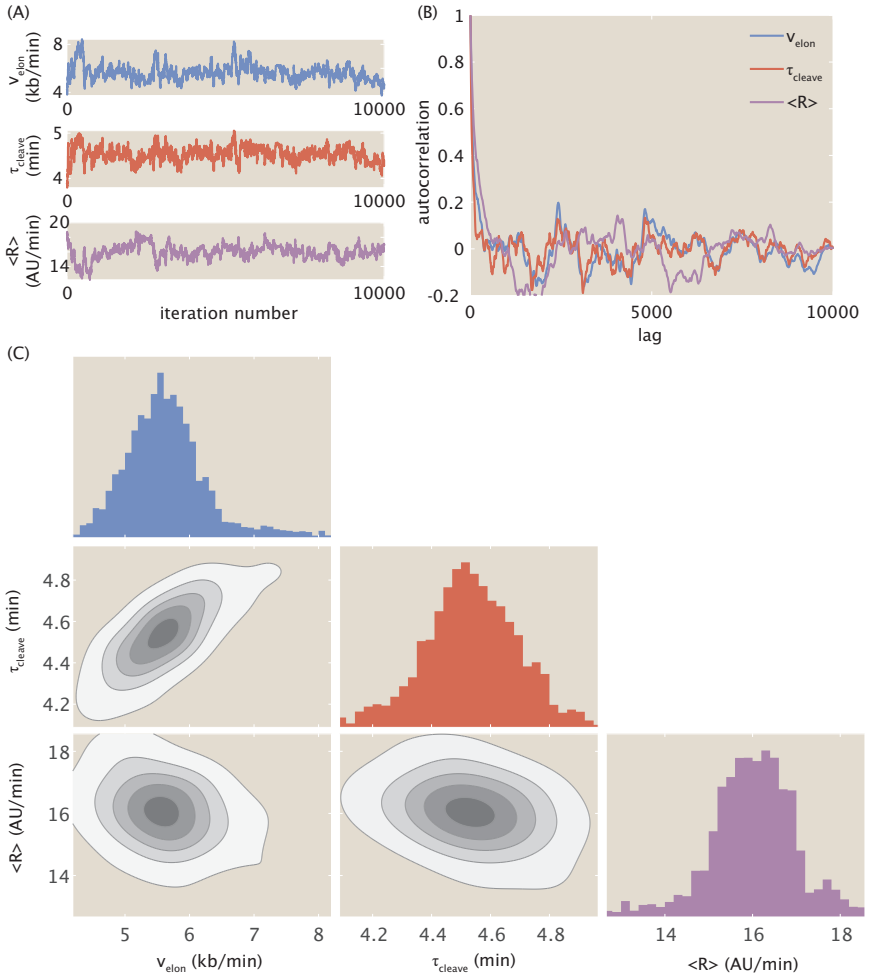

Figure S2. Diagnostics of MCMC inference procedure. (A) Raw chains for elongation rate v_{elon}, cleavage time τ_{cleave}, and mean initiation rate $\langle R \rangle$ for the inference results of a sample single cell. (B) Autocorrelation function for the raw chains in (A). (C) Corner plot of the same raw chains.

for reliably estimating the elongation rate while still analyzing the whole time window of data to be able to measure the other parameters such as the cleavage time.

S3.3 Curation of inference results

Individual single cell inference results were filtered automatically and then curated manually for final quality control. First, due to experimental and computational imaging limits, some MS2 or PP7 trajectories were too short to run a meaningful inference on. As a result, we automatically skipped over any cell with an MS2 or PP7 signal with fewer than 10 datapoints. This amounted to 260 cells skipped out of a total of 1053, with 567 (54%) retained.

Second, some single cells yielded poor fits, due to effects such as low signal-to-noise ratio. For example, some single-cell fluorescent signals did not capture enough of the early part of the nuclear cycle, resulting in ambiguity over when the locus actually began transcribing (Fig. S3E). In such cases, the resulting inferred parameter values were not reliable, and we rejected these fits. Additionally, the model failed to fit to the some fluorescent traces (Fig. S3F). For these cases, we surmised that this poor fit could be due to a multitude of factors, ranging from experimental acquisition noise to intrinsic biological deviation from the model. Due to our inability to further resolve these details, there was no one-size-fits-all approach to automatically filtering these inference results, and so we opted for conservative manual curation, retaining only the fits that were decent.

In sum, 299 cells of data were retained out of 567 total after this curation process. We reasoned that, since we still ended up with hundreds of single cells of data, the resultant statistical sample size was large enough to extract meaningful conclusions. To verify that the curation process did not introduce substantial bias into our results, we compared the mean inferred transcription cycle parameters from the 299 curated cells with those from the entire 567 cells, both curated and uncurated (Fig. S3G). The inferred results were nearly identical, with a minor systematic decrease in the mean initiation rate and cleavage time in the case of the uncurated results that nevertheless did not alter any position-dependent trends. Thus, we were confident that the curated dataset constituted a representative sample of the whole embryo.

S3.4 Validation of inference results

To assess the accuracy of the inference method, we validated our MCMC approach against a simulated dataset. Using the inferred distribution of model parameters from the experimental data, we generated a simulated dataset with our theoretical model (Section S1) and ran the MCMC inference on it.

The simulated dataset consisted of 100 cells. The model parameters used to simulate each individual cell's MS2 and PP7 fluorescences were drawn randomly from a Gaussian distribution, with mean μ and standard deviation σ calculated from the distribution of inferred model parameters from the experimental data. Table S1 shows the parameters used in the Gaussian distributions generating each single cell's model parameters.

In addition, fluorescence measurement error was generated by drawing a Gaussian random number with mean 0 and standard deviation 40 AU for each time point of data, for each single cell, and adding this random number to the MS2 or PP7 fluorescence at that time point (prior to rescaling the MS2 fluorescence with the scaling factor α).

After fitting with the MCMC procedure, the data were curated according to the protocol outlined in Section S3.3. 76 cells were retained out of a total of 100 simulated cells, with the 24 discarded cells exhibiting poor fits. These traces presented the same problems as their experimental counterparts described in Section S3.3, such as poor signal-to-noise. Figure S4A shows an example of the simulated MS2 and PP7 fluorescence from a single cell along with their corresponding fits. The resulting MCMC-sampled values of the mean initiation rate, elongation rate, and cleavage time are shown in the histograms in Figure S4B (blue), along with the ground truth for that single cell (red

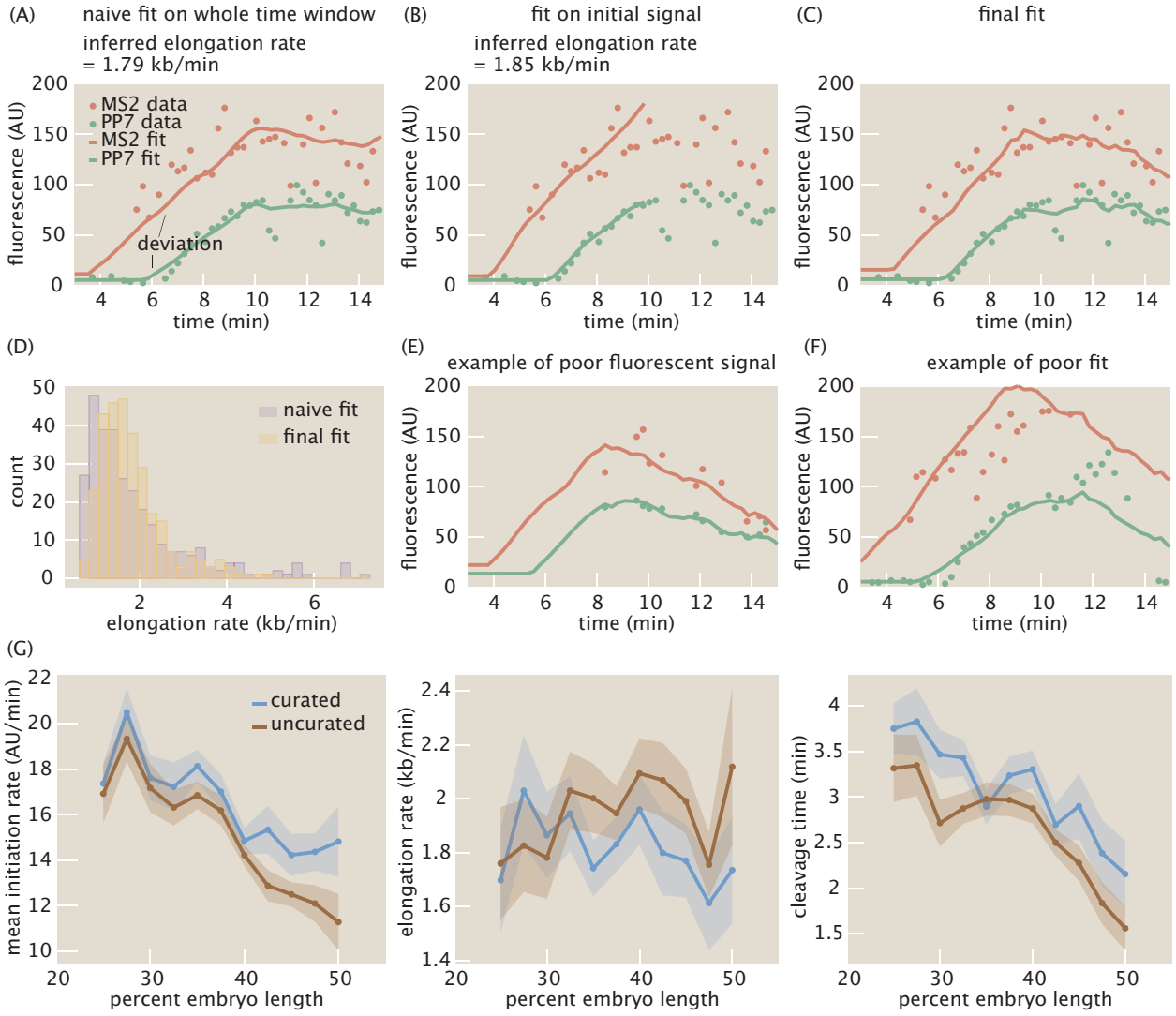

Figure S3. Overview of hierarchical fit and curation process. (A) Naive inference run on the entire 18 min time window showing a deviation of the fit from data at early time points (black lines). (B,C) Hierarchical fit where inference is run on (B) initial 10 min time window, yielding a more accurate measure of the elongation time, which is then held fixed for the final fit on the (C) entire 18 min time window. (D) Distribution of single-cell inferred elongation rate values using naive (purple) or hierarchical (yellow) fit schemes. (E, F) Examples of rejected fits due to (E) poor fluorescent signal quality in the beginning of the nuclear cycle, or (F) poor fit results. (G) Mean inferred transcription cycle parameters as a function of embryo position, for curated (blue) and uncurated (brown) data. Shaded regions represented standard error of the mean.

	mean (μ)	standard deviation (σ)
$\langle R \rangle$	16.6 AU/min	5.1 AU/min
v_{elon}	1.8 kb/min	0.8 kb/min
τ_{cleave}	3.1 min	1.4 min
t_{on}	3.5 min	1.6 min
α	0.16	0.05
$MS2_{basal}$	50 AU	10 AU
$PP7_{basal}$	50 AU	10 AU

Table S1. Mean and standard deviation of model parameters used in single-cell simulations.

line). As described in Section S3.1, the mean value of each sampled distribution was retained for downstream statistical analysis.

The accuracy of the inference was investigated on three levels: 1) systematic errors affecting mean analyses, 2) random errors affecting measurements of distributions, and 3) spurious correlations between parameters affecting inter-parameter correlations.

First, the scaled error ε for each parameter was calculated on a single-cell basis as defined by

$$\varepsilon = \frac{x_{infer} - x_{truth}}{\mu_x}, \tag{S16}$$

where x represents the model parameter being investigated, the subscripts indicate whether the quantity is the inferred result or the ground truth for that single cell, and μ_x is the population mean of the parameter value from the experimental data (i.e., the values of the "mean" column in Table S1). For example, for the mean initiation rate $\langle R \rangle$, $\mu_{\langle R \rangle}$ takes the value 16.6 AU/min. ε gives a unitless measure of the magnitude of inference error of each single cell, where a value of 1 indicates an error that is as large as the population mean itself.

Figure S4C shows the histogram of single-cell scaled errors $\varepsilon_{\langle R \rangle}$, $\varepsilon_{v_{elon}}$, and $\varepsilon_{tau_{cleave}}$ for the inferred mean initiation rate, elongation rate, and cleavage time, respectively. The majority of the scaled errors fall between -0.5 and 0.5, indicating that most inferred results possess relatively small error.

The systematic error on measurements of the ensemble mean can be estimated by calculating the mean of the scaled errors shown in Figure S4C. Doing so results in a value of 0.03 ± 0.03, 0.003 ± 0.03, and -0.09 ± 0.03 (mean and SEM) for the mean scaled error of the mean initiation rate, elongation rate, and cleavage time, respectively. For context, this means that, if the mean cleavage time is ~ 3 min, then the systematic error in the cleavage time is ~ 20 sec, about the time resolution of the data. Thus, the systematic error for each parameter is several orders of magnitude below that of the experimental mean value of each parameter, indicating that the inference provides an accurate and precise readout of the mean.

While the inference's systematic error may be small, the presence of random errors will affect measurements of distributions of parameters. To investigate the impact of these random errors, we quantified the fraction of total measured experimental variability that consisted of random inference error. Specifically, for a parameter x, we separated the variance of single-cell measurements as

$$\sigma^2_{x,total} = \sigma^2_{x,true} + \sigma^2_{x,random}, \tag{S17}$$

where $\sigma^2_{x,total}$ represents the overall single-cell variability observed in the data, $\sigma^2_{x,random}$ represents the random error inherent to our inference process, and $\sigma^2_{x,true}$ represents the true variability after subtracting out random inference error $\sigma^2_{x,random}$. Note that $\sigma^2_{x,total}$ is the square of the values in the standard deviation column in Table S1.

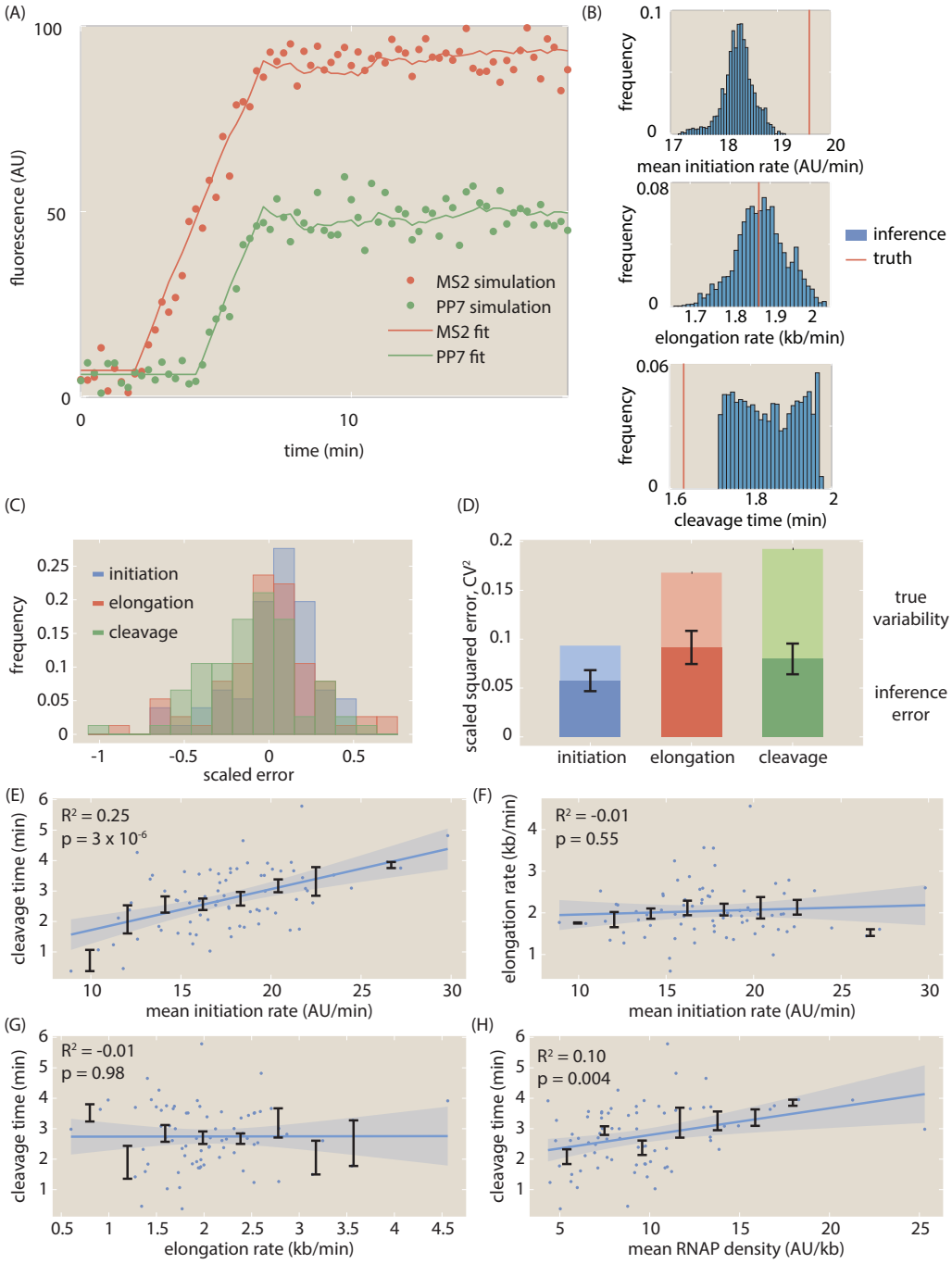

Figure S4. Overview of MCMC inference validation. (A) Example single-cell simulated data and inferred fits. (B) MCMC inference results for the simulated data in (A) for the mean initiation rate, elongation rate, and cleavage time. The histogram represents the raw MCMC sampled values, and the red line is the ground truth for this particular cell. The mean value of each histogram is then retained for further statistical analysis. (C) Scaled error of initiation, elongation, and cleavage for each simulated cell. (D) Comparison of relative magnitudes of random inference error and true experimental variability for the initiation, elongation, and cleavage parameters. (E, F, G, H) Single-cell correlations for simulated data between mean initiation rate and cleavage time, mean initiation rate and elongation rate, elongation rate and cleavage time, and mean RNAP density and cleavage time, respectively.

Dividing by the squared population means μ yields

$$\frac{\sigma^2_{x,total}}{\mu^2_x} = \frac{\sigma^2_{x,true}}{\mu^2_x} + \frac{\sigma^2_{x,random}}{\mu^2_x}. \tag{S18}$$

Note that these are just squared CV terms, and that the last term is simply the square of the scaled error ε defined earlier

$$CV^2_{x,total} = CV^2_{x,true} + \varepsilon^2_x. \tag{S19}$$

Thus, the overall impact of the inference's random error can be quantified by calculating the relative magnitudes of the contributions of $CV^2_{x,true}$ and ε^2 to the total variability $CV^2_{x,total}$. Figure S4D shows this separation, where the dark bars represent the squared scaled error ε^2, the light bars represent the true variability $CV^2_{x,true}$, and the overall bars represent the total variability $CV^2_{x,total}$ obtained from the values of μ and σ in Table S1.

All three model parameters—initiation, elongation, and cleavage—possess no more than approximately 50% random error. Nevertheless, the presence of this much error indicates that measurements of distributions of these parameters will be confounded by the random error present in our inference method, highlighting the general difficulty in measuring values beyond the mean. However, these errors in the inference of the variability of the transcription cycle parameters should not impact the results of investigating the distribution of elongation rates in Figure 2F, since the the widths of the simulated distributions in the presence or absence of single-molecule elongation variability differed by essentially an order of magnitude (see Section S9 for details).

Future improvements on increasing the accuracy of measurements of distributions could be achieved, for example, by utilizing interleaved loops such as those introduced in Figure S5. Here, two orthogonal species of mRNA binding proteins fused to different fluorescent proteins would bind to interleaved loops located at the 5′ end of the construct. In addition, a second pair of mRNA binding proteins would bind to an analogous set of interleaved loops located at the 3′ end. The result would be a four-color experiment, with two colors reporting on transcription at the 5′ end of the transcript, and two different colors reporting on transcription the 3′ end. In this scenario, the data would provide independent readouts of the same underlying signal, making it possible to perform two independent inferences on the same nucleus. This would allow for the decomposition of the inference into biological variability and inferential error using techniques analogous to those presented in S7.

Finally, we examined the inference method for spurious correlations to investigate the accuracy of the experimental single-cell correlations shown in Figure 3. The presence of spurious correlations would reflect inherent couplings in the inference method itself, since the simulation parameters were generated independently and stochastically.

Figure S4E-H show the single-cell correlations using a generalized linear regression between model parameters for the simulated dataset, as well as between the mean RNAP density and the cleavage time, as defined in the main text. We discovered a positive correlation (adjusted $R^2 = 0.25$) between the mean initiation rate and the cleavage time (Fig. S4E, $p = 3 \times 10^{-6}$). In contrast, there was no significant correlation between the mean initiation rate and elongation rate (Fig. S4F, adjusted $R^2 = -0.01$ and $p = 0.55$) or between the elongation rate and cleavage time (Fig. S4G, adjusted $R^2 = -0.01$ and $p = 0.98$). There was also a slight positive correlation between the mean RNAP density and the cleavage time, with adjusted $R^2 = 0.10$ and $p = 0.004$ (Fig. S4H). Nevertheless, these spurious correlations were actually the *opposite* of the correlations discovered in the experimental data, which exhibited a *negative* correlation between the mean initiation rate and cleavage time, as well as between the mean RNAP density and cleavage time. The comparisons of adjusted R^2 and p-values between the data and simulations are summarized in Table S2.

Thus, our results validated the single-cell correlations discovered in the main text, since the simulated inference results either found no correlation or the opposite correlation of that found

	initiation / cleavage	initiation / elongation	elongation / cleavage	RNAP density / cleavage
data	$R^2 = 0.10$ $p = 1 \times 10^{-8}$ negative correlation	$R^2 = 0.01$ $p = 0.08$ insignificant correlation	$R^2 = 0.10$ $p = 1 \times 10^{-7}$ positive correlation	$R^2 = 0.18$ $p = 5 \times 10^{-15}$ negative correlation
simulation	$R^2 = 0.25$ $p = 3 \times 10^{-6}$ positive correlation	$R^2 = -0.01$ $p = 0.55$ insignificant correlation	$R^2 = -0.01$ $p = 0.98$ insignificant correlation	$R^2 = 0.10$ $p = 0.004$ positive correlation

Table S2. Comparison of adjusted R^2 and p-values between experimental and simulated single-cell correlations.

in the actual data, indicating that the experimental results were not the product of spurious correlations.

S4 Calibration of MS2 and PP7 signals

In the inference scheme presented in the main text, we allowed the scaling factor between the MS2 and PP7 fluorescence signals to be a free model parameter. Allowing this scaling factor to be a free parameter facilitates adoption of the method and obviates the need for an external control measurement to calibrate the MS2 and PP7 signals. Here, we show that the inferred scaling parameter is comparable to that resulting from such calibration measurements.

Due to the fact that the MS2 and PP7 stem loop sequences were associated with mCherry and eGFP fluorescent proteins, respectively, the two experimental fluorescent signals possessed different arbitrary fluorescent units, related by the scaling factor α

$$\alpha = \frac{F_{MS2}}{F_{PP7}}, \tag{S20}$$

where F_{MS2} and F_{PP7} are the fluorescence values generated by a fully transcribed set of MS2 and PP7 stem loops, respectively. Although α has units of $AU_{\text{MS2}}/AU_{\text{PP7}}$, we will express α without units in the interest of clarity of notation. The value of α was inferred as described above in Section S3. As an independent validation, we measured α by using another two-color reporter, consisting of 24 alternating, rather than sequential, MS2 and PP7 loops (***Wu et al., 2014***; ***Chen et al., 2018***) inserted at the 5′ end of our reporter construct (Fig. S5A).

Figure S5B shows a representative trace of a single spot containing our calibration construct. For each time point in nuclear cycle 14, the mCherry fluorescence in all measured single-cell traces was plotted against the corresponding eGFP fluorescence (Fig. S5C, yellow points). The mean α was then calculated by fitting the resulting scatter plot to a line going through the origin (Fig. S5C, black line). The best-fit slope yielded the experimentally calculated value of $\alpha = 0.154 \pm 0.001$ (SEM). A distribution for α was also constructed by dividing the mCherry fluorescence by the corresponding eGFP fluorescence for each datapoint in Figure S5D, yielding the histogram in Figure S5D (yellow), which possessed a standard deviation of 0.0733.

Binning the cells by position along the embryo revealed a slight position dependence in the scaling factor, with higher values of α in the anterior, about 0.15, and lower values in the posterior, about 0.1 (Fig. S5E, yellow).

We then compared the values of α from the single-cell inference in the main text to those of the control experiment. Figure S5D shows a histogram of inferred values of α from the inference procedure (blue), with a mean of 0.161 ± 0.003 (SEM) and a standard deviation of 0.049, in agreement with the independent measurement described above. Furthermore, the inference revealed the

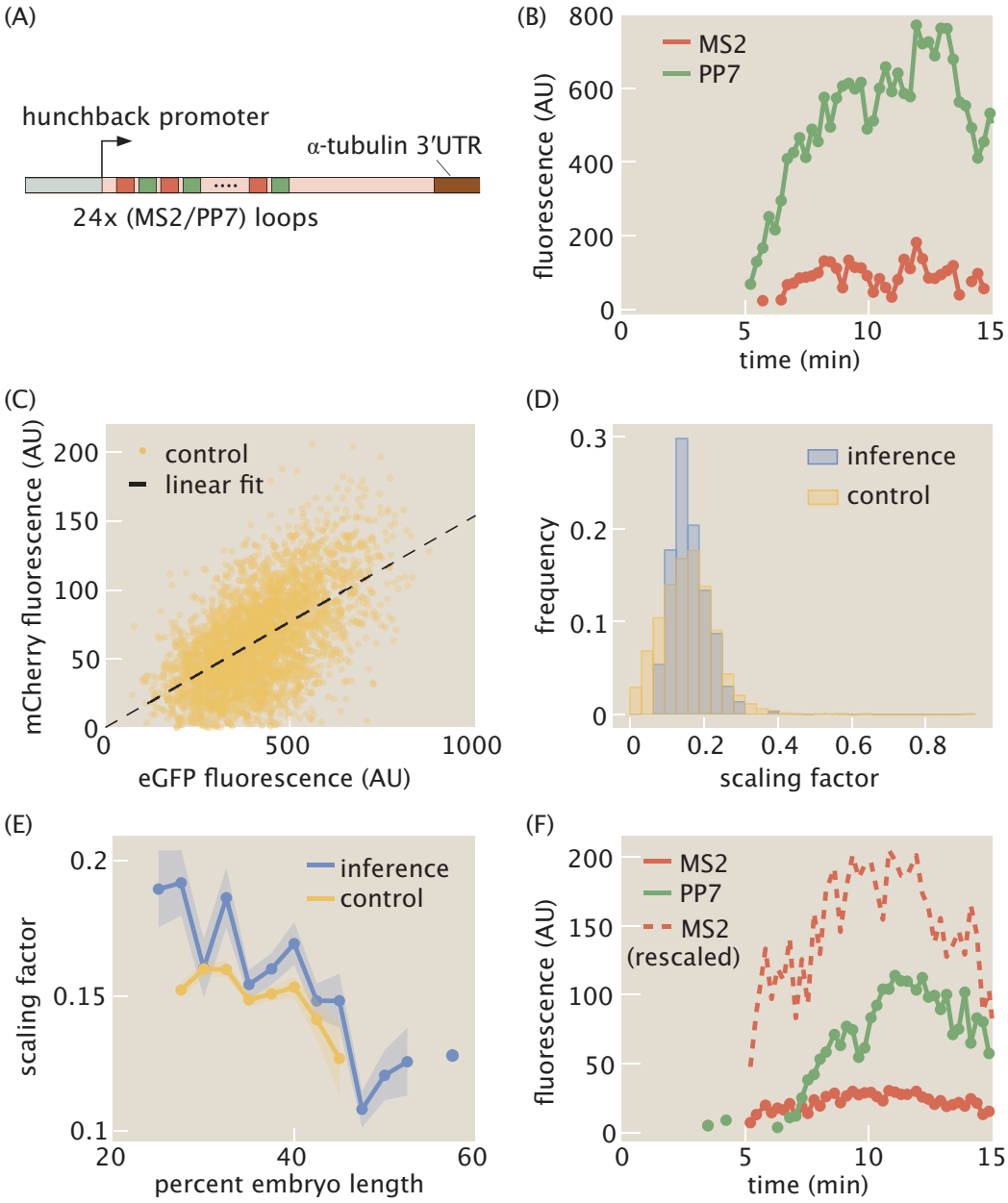

Figure S5. Calibration of MS2 and PP7 fluorescence signals. (A) Schematic of construct used to measure the scaling factor α using interlaced MS2/PP7 loops. (B) Sample single-cell MS2 and PP7 traces from this control experiment. (C) Scatter plot of MS2 and PP7 fluorescence values for each time point along with linear best fit resulting in $\alpha = 0.154 \pm 0.001$. (D) Histogram of inferred values of α at the single-cell level from data in the main text, along with histogram of α values from the control experiment. (E) Position-dependent mean value of α in both the main text inference and the control experiment. (F) Representative raw and rescaled MS2 and PP7 traces for a sample single cell in the main text data set. (C,D,E, data were collected for 314 cells across 4 embryos for the control experiment, and for 299 cells across 7 embryos for the experiment from the main text; shaded regions in E reflect standard error of the mean.)

same position-dependent trend as the control experiment, with higher mean values of α in the anterior of the embryo (Fig. S5E, blue line).

The position dependence observed both in the calibration experiments and inference suggests that this spatial modulation in the value of α is not an artifact of the constructs or our analysis, but a real feature of the system. We speculated that this spatial dependence could stem from differential availability of MCP-GFP and PCP-GFP along the embryo, leading to a modulation in the maximum occupancy of the MS2 stem loops versus the PP7 stem loops. Regardless, our data demonstrate that the inferred and calibrated α can be used interchangeably.

With the inference of α validated against the independent control calculation, the MS2 signals for each single cell could be rescaled to the same units as the PP7 signal (Fig. S5F). All plots in the main text and supplementary information, unless otherwise stated, reflect these rescaled values using the overall mean value of $\alpha = 0.1539$ obtained from the inference.

S5 Validation of the RNAP processivity assumption

The calibration between the MS2 and PP7 (Section S4) signals provided an opportunity to test the processivity assumption presented in the main text, namely that the majority of loaded RNAP molecules transcribe to the end of the gene without falling off. To estimate the processivity quantitatively, we assume that a series of N RNAP molecules transcribes past the MS2 stem loop sequence at the 5′ end of the reporter gene, and that only pN successfully transcribe past the PP7 stem loop sequence at the 3′ end. Here, we define p to be the processivity factor, and require $0 < p < 1$. Thus, $p = 1$ indicates maximal processivity where every RNAP molecule that transcribes the MS2 sequence also transcribes the PP7 sequence, and $p = 0$ indicates minimal processivity, where no RNAP molecules make it to the PP7 sequence.

We assume that no RNAP molecules fall off the gene while they transcribe the interlaced MS2/PP7 loops used in the calibration experiment described in Figure S5A. Under this assumption, N RNAP molecules will fully transcribe both sets of stem loop sequences, allowing us to define the scaling factor as the ratio of total fluorescence values

$$\alpha_{\text{calib}} = \frac{NF_{MS2}}{NF_{PP7}} = \frac{F_{MS2}}{F_{PP7}}. \tag{S21}$$

Note that, in this simple model, RNAP molecules can still fall off the gene after they transcribe the set of MS2/PP7 loops. Now, we consider the construct with MS2 and PP7 at opposite ends used in the main text. Allowing a fraction p of RNAP molecules to fall off the gene between the MS2 and PP7 loops, we arrive at a scaling factor

$$\alpha_{\text{infer}} = \frac{NF_{MS2}}{pNF_{PP7}} = \frac{F_{MS2}}{pF_{PP7}}. \tag{S22}$$

We can thus calculate the processivity p from taking the ratio of the true and biased scaling factors

$$p = \frac{\alpha_{\text{calib}}}{\alpha_{\text{infer}}}. \tag{S23}$$

Taking the mean value of α_{calib} from our control experiment to be the true value and the mean value of α_{infer} from the inference from the main text to be the biased value, we calculate a mean processivity of $p = 0.96$, with a negligible standard error of 4.81×10^{-5}. Thus, on average, 96% of RNAP molecules that successfully transcribe the 5′ MS2 stem loop sequence also successfully transcribe the 3′ PP7 stem loop sequence, confirming previous results (***Garcia et al., 2013***) and lending support to the processivity assumption invoked in our model.

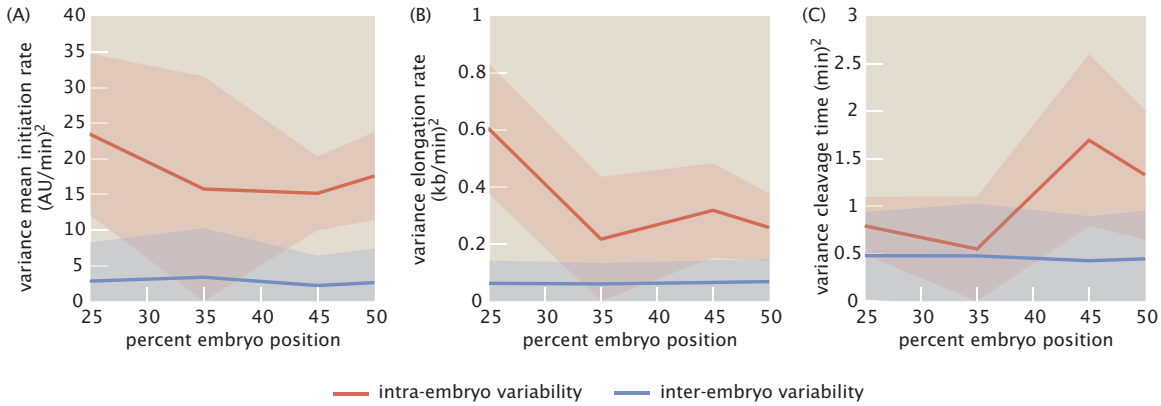

Figure S6. Comparison of intra- and inter-embryo variability for inferred (A) mean initiation rates, (B) elongation rates, and (C) cleavage times, as a function of embryo position. Data were taken over 299 cells across 7 embryos, with approximately 10-90 cells per embryo in the region of the embryo examined here.

S6 Comparing intra- and inter-embryo variability

In the analysis in the main text, we treated all single cell inference results equally within one statistical set. In principle, this is justified only if the variability between single cells is at least as large as the variability between individual embryos. In this section we prove this assumption.

Here, we examine two quantities: the *intra-embryo variability*, defined as the variance in a parameter across all single cells in a single embryo, and the *inter-embryo variability*, defined as the variance across embryos in the single-embryo mean of a parameter. We examined these two quantities for the three primary inferred parameters – the mean initiation rate, elongation rate, and cleavage time.

Figure S6 shows the results of this comparison, where the red (blue) lines indicate the intra- (inter-) embryo variability and the red (blue) shaded regions indicate the standard error (bootstrapped standard error) in the intra- (inter-) embryo variability. For all of the parameters, the intra-embryo variability is at least as large as the inter-embryo variability, validating our treatment of all of the single-cell inference results as a single dataset, regardless of embryo.

S7 Comparison of variability in mean initiation rate reported by our inference with static measurements

A widespread strategy to measure variability in transcription initiation relies on techniques such as single-molecule FISH (smFISH), which count the number of nascent transcripts at a transcribing locus in a fixed sample (***Femino et al., 1998***; ***Raj et al., 2006***; ***Zenklusen et al., 2008***; ***Little et al., 2013***; ***Zoller et al., 2018***). These single time point measurements are typically interpreted as reporting on the cell-to-cell variability in transcription initiation. Further, under the right conditions, the variability reported by this method has been shown to be dominated by biological sources of variability and to have a negligible contribution from experimental sources of noise (***Zoller et al., 2018***).

We sought to determine how well our approach could report on biological variability. To do so, we contrasted the inference results of the transcriptional activity of our *hunchback* reporter with a snapshot-based analysis inspired by single-molecule FISH (***Zoller et al., 2018***). Specifically, we calculated the CVs in the raw MS2 and PP7 fluorescence in snapshots taken at 10 minutes after the start of nuclear cycle 14. We reasoned that, since this calculation does not utilize the full time-resolved nature of the data, it provides a baseline measurement of total noise that encompasses both experimental and biological variability. As a point of comparison, we also calculated the CV in the instantaneous MS2 signal from another work using a similar P2P-MS2-lacZ construct (***Eck et al.,***

2020).

Figure S7A shows the CV as a function of embryo position as reported by these different approaches. For the static measurements (red, green, and blue), the CV lay around 20% to 40%, reaching a peak near 40% along the length of the embryo. The CV of the inferred mean initiation rate (purple) exhibited similar values, although it was slightly lower in a systematic fashion. This difference was likely due to the fact that the inference relies on time-dependent measurements that can average out certain sources of error such as experimental noise, whereas such time averaging is not possible in the context of single time point measurements.

To test whether the discrepancy in the CV between time-resolved and snapshot-based measurements arose from differences in the experimental error of each technique, we utilized the alternating MS2-PP7 reporter used in the calibration calculation (Section S4) to separate out experimental sources of variability from true biological sources. Specifically, because the MS2 and PP7 fluorescent signals in this reporter construct should, in principle, reflect the same underlying biological signal, deviations in each signal from each other should report on the magnitude of the experimental error.

Following the formalism introduced by ***Elowitz et al.*** (***2002***), we identify the correlated noise between the MS2 and PP7 signals as true biological variability. In contrast we identify the uncorrelated noise with experimental variability. We then used the two-color formalism (***Elowitz et al., 2002***) to separate out experimental noise from biological noise using the MS2 and PP7 fluorescent signals at each point in time presented in Figure S5C . First, we defined the deviations δ_{MS2} and δ_{PP7} of each instantaneous MS2 and PP7 fluorescent signal from the mean MS2 and PP7 fluorescence signals, averaged across nuclei and time

$$\delta_{MS2} = \frac{F_{MS2}}{\langle F_{MS2} \rangle} - 1 \tag{S24}$$

$$\delta_{PP7} = \frac{F_{PP7}}{\langle F_{PP7} \rangle} - 1, \tag{S25}$$

where F_{MS2} and F_{PP7} are the instantaneous MS2 and PP7 fluorescences for a given nucleus and time point, respectively, and $\langle F_{MS2} \rangle$ and $\langle F_{PP7} \rangle$ are the mean MS2 and PP7 fluorescences, averaged across nuclei and time points, respectively. Using these deviations, the uncorrelated and correlated noise terms are defined as

$$\eta^2_{uncorr} = \frac{1}{2}\langle (\delta_{MS2} - \delta_{PP7})^2 \rangle \tag{S26}$$

$$\eta^2_{corr} = \langle \delta_{MS2} \delta_{PP7} \rangle, \tag{S27}$$

where the brackets indicate an ensemble average over time points and cells. From this, the total noise η^2_{tot}, defined as the variance σ^2 divided by the mean squared μ^2, is simply the uncorrelated and correlated noise components added in quadrature

$$\eta^2_{tot} = \frac{\sigma^2}{\mu^2} = \eta^2_{uncorr} + \eta^2_{corr}. \tag{S28}$$

Note that the total noise η^2_{tot} is simply the squared coefficient of variation. Thus, the squared coefficient of variation (CV^2) of our data is equal to η^2_{tot} and can be separated into the uncorrelated and correlated components.

Figure S7B shows this CV^2 (averaged across embryo position) compared with the separated uncorrelated and correlated noise sources. Intriguingly, the uncorrelated and correlated noise (yellow) each contribute about half to the overall noise, which is quantitatively comparable to the CV^2 of the static snapshot of MS2 and PP7 data used in the main text (red, green), roughly 20%. Furthermore, the CV^2 of the inferred mean initiation rate is roughly half of the CV^2 of the static fluorescence measurements and is quantitatively comparable to the correlated noise, at about 10%.

As a result, the MCMC inference method can quantitatively capture the true biological variability in the mean initiation rate while separating out the uncorrelated contribution due to experimental noise. Thus our results support the power of model-driven inference approaches in providing clean readouts of variability in transcriptional parameters.

S8 Comparison of distribution of elongation rates with other works

As an additional validation of our inference results, we compared the distribution of single-cell inferred elongation rates with those reported in two similar works by ***Hocine et al.*** (***2013***) and ***Fukaya et al.*** (***2017***). Both of these works used a two-color live imaging reporter like the one utilized in this work, and measured the time delay between the onset of each stem loop signal to estimate a single-cell mean elongation rate. ***Fukaya et al.*** (***2017***) studied a similar *hunchback* reporter to the one used here, while ***Hocine et al.*** (***2013***) used a reporter construct in yeast.

Figure S8 shows the comparison of distributions of elongation rates. Because the reporter constructs and analysis techniques differed between works, a quantitative comparison is not possible. Nevertheless, all three sets of results report a significant cell-to-cell variability in mean elongation rate, ranging from 1 kb/min to 3 kb/min.

S9 Theoretical investigation of single-cell distribution of elongation rates

To investigate the molecular mechanisms underling single-cell distributions of elongation rates obtained from the inference, we developed a single-molecule theoretical model. We were interested in how the observed variability in single-cell elongation rates could constrain models of the single-molecule variability in RNAP elongation rates. To disregard effects due to position-dependent modulations in the transcription initiation rate, we only studied cells anterior of 40% along the embryo length, where the initiation rate was roughly constant.

The model was adapted from the stochastic Monte Carlo simulation used in ***Klumpp and Hwa*** (***2008***), which accounts for the finite size of RNAP molecules (Fig. S9). Here, single RNAP molecules are represented by one-dimensional objects of size $N_{footprint}$ that traverse a gene consisting of a one-dimensional lattice with a total number of sites, corresponding to single base pairs, equal to N_{sites}. The position of the active site of molecule i is given by x_i, which takes integer values—each integer corresponds to a single base pair of the gene lattice. Because RNAP molecules have a finite size, given by $N_{footprint}$, an RNAP molecule i thus occupies the lattice sites from x_i to $x_i + N_{footprint}$.

New RNAP molecules are loaded at the start of the gene located at $x = 0$. Due to the exclusionary interactions between molecules, simultaneously simulating the motion of all molecules is unfeasible, and a simulation rule dictating the order of events is necessary. At each simulation timestep dt, a randomized sequence of indices is created from the following sequence

$$\mathcal{I} = \{0, 1, \dots, N\}, \tag{S29}$$

where $\{1, \dots, N\}$ correspond to any RNAP molecules $i = 1, \dots, N$ already existing on the gene, and 0 corresponds to the promoter loading site for new RNAP molecules. The process is repeated until a total simulation time T has elapsed.

Choosing indices i from the random sequence $\mathcal{I}$ obtained above, the following actions are taken. If the promoter loading site is chosen ($i = 0$), an RNAP molecule is loaded with probability β, only if no already existing RNAP molecules overlap with the footprint of the new RNAP molecule. If such an overlap occurs, then no action is taken. To calculate the probability of loading, a random number is drawn from a Poisson distribution with parameter $\beta\, dt$. Recall that, for a Poisson distribution with parameter $\beta\, dt$, the resulting random variable corresponds to the number of occurrences in a time frame dt. Here, if this number is one or higher, then the loading event is considered a success.

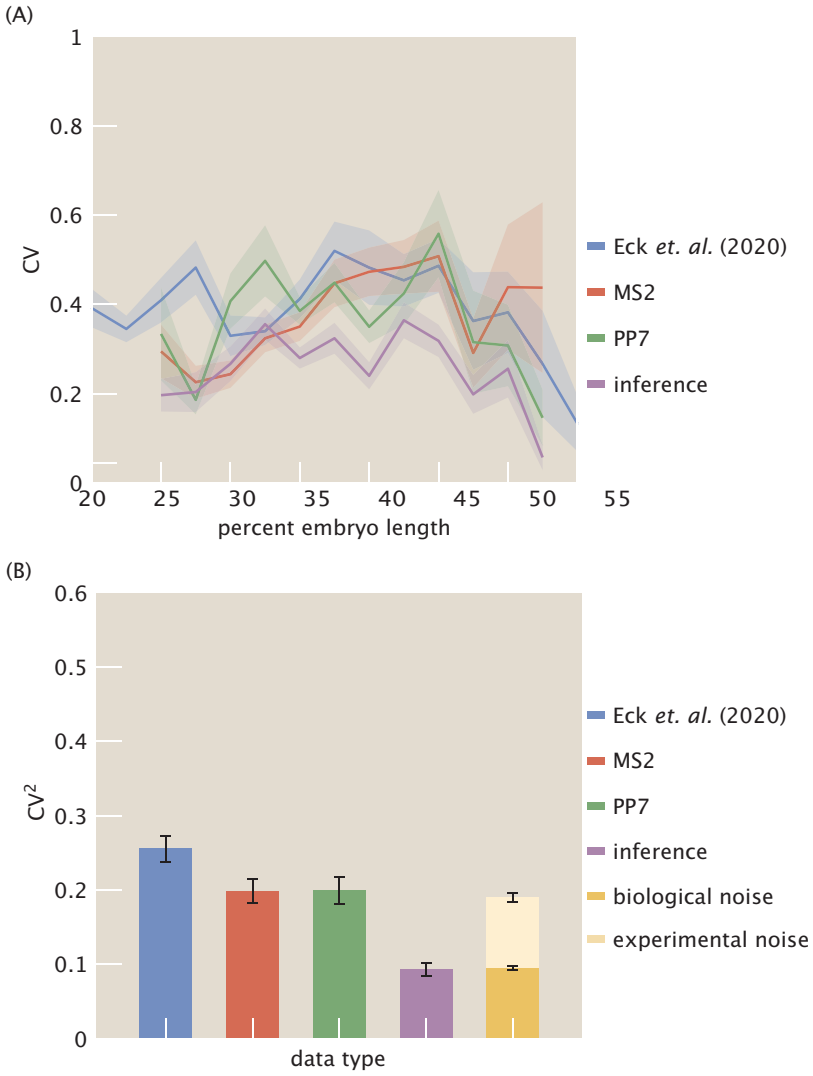

Figure S7. Comparison of coefficients of variation (CV) between inferred mean initiation rates and instantaneous counts of number of nascent RNA transcripts. (A) Position-dependent CV of inferred mean initiation rate (purple) compared with static measurements of MS2 and PP7 raw fluorescence (red, green), as well as with static measurements of MS2 data from ***Eck et al.*** (***2020***). (B) Position-averaged squared CVs of the same measurements, where the entire dataset is treated as a single sample and embryo position information is disregarded. In addition, separation of experimental (uncorrelated) and biological (correlated) sources of variability are shown, calculated using the reporter described in Section S4. (A, Shaded regions indicate bootstrapped standard error of the mean; B, error bars indicate bootstrapped standard error of the mean.)

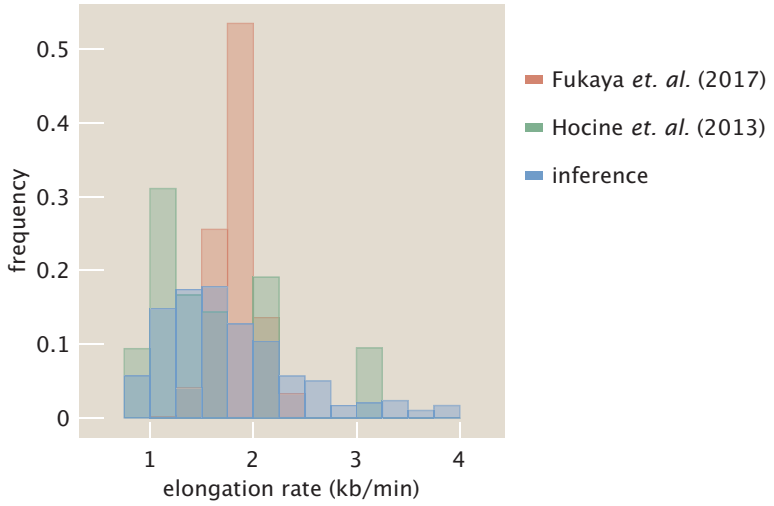

Figure S8. Comparison of distribution of elongation rates (green) with previous studies (***Hocine et al.*** (***2013***), red and ***Fukaya et al.*** (***2017***), blue). Distributions of previous studies were adapted from Figs. 2D and 2A of ***Hocine et al.*** (***2013***) and ***Fukaya et al.*** (***2017***), respectively.

If the index i indicates that an RNAP molecule was chosen $i > 0$, then that RNAP molecule advances forward with stochastic rate ϵ. This probability is simulated by drawing a random number from a Poisson distribution with parameter $\epsilon\ dt$, thus giving an expected distance traveled of $\epsilon\ dt$ per timestep. If this movement would cause the RNAP molecule to overlap with another RNAP molecule, then no action is taken. Otherwise, the RNAP molecule moves forward the number of steps given by the generated random variable.

To simulate potential single-molecule variability, each RNAP molecule can possess a different stepping rate ϵ. For a given RNAP molecule i, its stochastic stepping rate ϵ_i is drawn from a truncated normal distribution Tr with mean μ_ϵ and standard deviation σ_ϵ and lower and upper limits 0 and infinity, respectively

$$\epsilon_i = Tr(\epsilon, \sigma_\epsilon, 0, \infty). \tag{S30}$$

Once the position of the active site of an RNAP molecule exceeds that of the total number of sites N_{sites}, i.e. the molecule reaches the end of the gene, it is removed from the simulation. The simulation does not incorporate any cleavage or RNAP termination processes, since it only focuses on studying elongation dynamics in the body of the gene. Additionally, we do not incorporate sequence-dependent RNAP pausing along the gene.

To calculate a mean elongation rate, we first computed a mean elongation rate for each single RNAP molecule in the simulation. This single-molecule elongation rate was obtained by taking the finite difference in position divided by the timestep dt for each RNAP molecule loaded during a single simulation rate. Then, we averaged these single-molecule elongation rates to obtain a simulation-wide mean elongation rate.

We treated each simulation as an individual cell such that we interpreted this quantity as precisely the single-cell elongation rate inferred from the data in the main text. Thus, the distribution of mean elongation rates across a simulated population of cells was compared to the experimentally inferred distribution of single-cell elongation rates. The simulation was run for 200 cells.

Finally, to account for single-cell variability in the transcription initiation rate, the loading rate β was allowed to vary across each simulated cell j and was drawn from a Gaussian distribution with parameters reflecting the actual data. Since *hunchback* is known to load new nascent RNA transcripts at a rate of 1 molecule every 6 seconds in the anterior of the embryo (***Garcia et al.,***

Parameter	Description	Value
T	total simulation time	600 sec
dt	simulation timestep	0.5 sec
N_{sites}	size of lattice	6626 bp
$N_{footprint}$	RNAP footprint (***Selby et al., 1997***)	40 bp
μ_β	mean loading rate	0.17 sec^{-1}
σ_β	standard deviation of loading rate	0.05 sec^{-1}
μ_ϵ	mean elongation rate	free parameter
σ_ϵ	standard deviation of elongation rate	free parameter

Table S3. Parameters used in single-molecule Monte Carlo simulation of elongation rates.

2013), we thus chose the mean of this distribution μ_β to be 1 molecule$/6\ s = 0.17\ s^{-1}$. The standard deviation σ_β was chosen to be this mean multiplied by the CV in the initiation rate in the anterior inferred in the main text, resulting in a value of $0.05\ s^{-1}$. Thus, for simulated cell j

$$\beta_j = N(\mu_\beta, \sigma_\beta), \tag{S31}$$

where any negative value was replaced with zero.

The values of each simulation parameter are summarized in Table S3.

To investigate the nature of molecular variability in elongation rates, we attempted to fit the mean and variance of the simulated distribution of elongation rates with those of the inferred single-cell distribution from the data.

First, we fixed σ_ϵ to zero and left μ_ϵ as a free parameter (Fig. 2F, brown). Because here each RNAP molecule had the same stepping rate, the exclusionary interactions between molecules did not appear to substantially alter the single-cell mean elongation rate and the model could not produce the high single-cell variability in elongation rate seen in the data (Fig. 2F, blue).

In contrast, if we also left the single-molecule variability in elongation rate σ_ϵ as a free parameter, the model could reasonably produce the distribution observed in the data (Fig. 2F, gold). The model produced a simulated mean (standard deviation) of $1.83(0.75)$ kb/min compared to the inferred values of $1.84(0.75)$ kb/min from the data.

The best fit parameters were $\mu_\epsilon = 2.76$ kb/min and $\sigma_\epsilon = 3.72$ kb/min, indicating that substantial variability in the single-molecule elongation rate was necessary. In addition, the value of μ_ϵ was much larger than the overall mean elongation rate of 1.84 kb/min seen in the data, likely due to the fact that the high densities of RNAP molecules here resulted in traffic jams, effectively slowing down the overall single-cell elongation rate despite the high single-molecule stepping rates of each individual RNAP molecule.

S10 Supplementary Videos

S1. **Video 1. Measurement of reporter construct.** Movie of P2P-MS2-lacZ-PP7 reporter construct used in an embryo in nuclear cycle 14. Time is defined with respect to the previous anaphase.

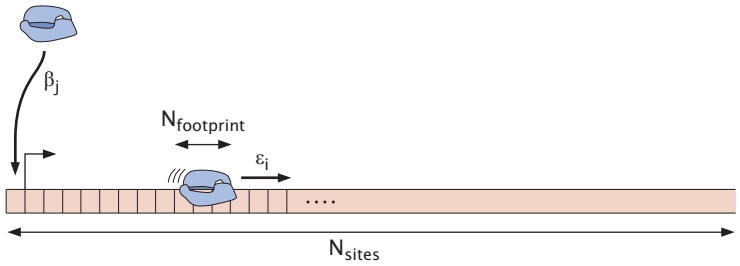

Figure S9. Cartoon overview of simulation. RNAP molecules with footprint $N_{footprint}$ stochastically advance one-dimensional gene represented as a lattice with N_{sites} unique sites, with each site equivalent to a single base pair. Each RNAP molecule i possesses an intrinsic stepping rate ϵ_i, and each cell j stochastically loads new RNAP molecules at the promoter with rate β_j.